Journal of Cardiovascular Magnetic Resonance 27 (2025) 101951

Contents lists available at ScienceDirect

Journal of Cardiovascular Magnetic Resonance

journal homepage: www.sciencedirect.com/journal/jocmr

Original Research

Optimizing cardiac diffusion tensor imaging in vivo: More directions or repetitions?

Sam Coveney[a], David Shelley[b], Richard J. Foster[a], Maryam Afzali[a,c], Ana-Maria Poenar[a], Noor Sharrack[a], Sven Plein[a], Erica Dall'Armellina[a], Jürgen E. Schneider[a,1], Christopher Nguyen[d,1], Irvin Teh[a,*,1]

[a] Leeds Institute of Cardiovascular and Metabolic Medicine (LICAMM), University of Leeds, Leeds, UK
[b] Leeds Teaching Hospitals NHS Trust, Leeds, UK
[c] Cardiff University Brain Research Imaging Centre (CUBRIC), School of Psychology, Cardiff University, Cardiff, UK
[d] Cleveland Clinic, Heart Vascular Thoracic Institute, Cardiovascular Innovation Research Center, Cleveland, Ohio, USA

ARTICLE INFO

Keywords:
Cardiac MRI
Diffusion tensor imaging
Diffusion schemes
Diffusion encoding directions
Heart
Myocardium

ABSTRACT

Background: Cardiac diffusion tensor imaging (cDTI) is sensitive to imaging parameters, including the number of unique diffusion encoding directions (ND) and number of repetitions (NR; analogous to number of signal averages). However, there is no clear guidance for optimizing these parameters in the clinical setting.

Methods: Spin echo cDTI data with second-order motion-compensated diffusion encoding gradients were acquired in 10 healthy volunteers on a 3T magnetic resonance imaging scanner with different diffusion encoding schemes in pseudo-randomized order. The data were subsampled to yield 96 acquisition schemes with $6 \leq ND \leq 30$ and $33 \leq$ total number of acquisitions (NA_{all}) ≤ 180. Stratified bootstrapping with robust fitting was performed to assess the accuracy and precision of each acquisition scheme. This was quantified across a mid-ventricular short-axis slice in terms of root mean squared difference (RMSD), with respect to the full reference dataset, and standard deviation (SD) across bootstrap samples, respectively.

Results: For the same acquisition time, the ND = 30 schemes had on average 48%, 40%, 34%, and 34% lower RMSD and 6.2%, 7.4%, 10%, and 5.6% lower SD in mean diffusivity (MD), fractional anisotropy (FA), helix angle (HA), and absolute sheetlet angle (|E2A|) compared to the ND = 6 schemes. Given a fixed number of high b-value acquisitions, there was a trend toward lower RMSD and SD of MD and FA with increasing numbers of low b-value acquisitions. Higher NA_{all} with longer acquisition times led to improved accuracy in all metrics, whereby quadrupling NA_{all} from 40 to 160 volumes led to *a* 20%, 39%, 11%, and 5.4% reduction in RMSD of MD, FA, HA, and |E2A|, respectively, averaged across six diffusion encoding schemes. Precision was also improved with *a* corresponding 53%, 50%, 53%, and 36% reduction in SD.

Conclusion: We observed that accuracy and precision were enhanced by (i) prioritizing number of diffusion encoding directions over NR given a fixed acquisition time, (ii) acquiring sufficient low b-value data, and (iii) using longer protocols where feasible. For clinically relevant protocols, our findings support the use of ND = 30 and NA_{b50}:$NA_{b500} \geq 1/3$ for better accuracy and precision in cDTI parameters. These findings are intended to help guide protocol optimization for harmonization of cDTI.

List of abbreviations: BPM, beats per minute; CI, confidence interval; DES, diffusion encoding scheme; DTI, diffusion tensor imaging; |E2A|, absolute sheetlet angle; EPI, echo planar imaging; FA, fractional anisotropy; HA, helix angle; IQR, interquartile range; M2, second-order motion-compensated; MD, mean diffusivity; NA, number of acquisitions; ND, number of diffusion encoding directions; NR, number of repetitions; RMSD, root mean squared difference; SCMR, Society for Cardiovascular Magnetic Resonance; SNR, signal-to-noise ratio; TE, echo time; TR, repetition time; SD, standard deviation

* Corresponding author.
E-mail address: i.teh@leeds.ac.uk (I. Teh).
[1] Joint senior authors.

https://doi.org/10.1016/j.jocmr.2025.101951
Received 8 February 2025; Received in revised form 10 July 2025; Accepted 26 August 2025

1. Introduction

Cardiac diffusion tensor imaging (cDTI) is a rapidly emerging technique for myocardial tissue characterization in vivo without the need for contrast agents [1]. It has shown promise in characterizing the microstructural changes in several clinical scenarios, including myocardial infarction [2–6], hypertrophic cardiomyopathy [7–11], aortic stenosis [12], amyloidosis [13], and others. The major challenge of cDTI for in vivo imaging is its high sensitivity to bulk motion of the heart during contracture. To ameliorate this, the use of second-order motion-compensated (M2) diffusion encoding gradients has become standard practice in spin echo planar imaging (EPI) [14,15]. This leads to longer echo times (TEs) and lower signal-to-noise ratio (SNR) compared to using non-motion-compensated diffusion gradients, which is compounded by the relatively short T_2 of the myocardium, i.e., ~44 ms at 3T [16].

To obtain adequate SNR and to mitigate instances of images containing artifacts, clinical cDTI protocols typically employ high number of repetitions ($8 \leq NR \leq 16$) [14,17,18]. We refer to NR instead of the more commonly used number of signal averages because cDTI data are in general exported and reconstructed offline as separate repetitions instead of being averaged on the scanner. However, the number of unique diffusion encoding directions ($6 \leq ND \leq 12$) [14,15,17–19] often remains small relative to diffusion tensor imaging (DTI) protocols used in other anatomy, such as the brain, where $ND \geq 30$ has been recommended [20]. As the imaging time is related to both NR and ND, identifying a suitable range of NR and ND is important for cDTI within a clinically feasible timeframe. Moreover, DTI parameters, including mean diffusivity (MD) and fractional anisotropy (FA), as measured in the healthy myocardium with spin echo methods are known to vary in the literature with reports of $0.75 \times 10^{-3}\ mm^2/s \leq MD \leq 1.72 \times 10^{-3}\ mm^2/s$ and $0.29 \leq FA \leq 0.43$ [17,19,21]. Known imaging sources of variation for these parameters include spatial resolution [22], ND, NR, SNR [23], diffusion encoding time [24], and b-value [18]. Isolating the effects of NR and ND is therefore an important aspect in the optimization of efficient and robust cDTI protocols for clinical use.

In DTI, $ND = 6$ is the minimum number of unique non-zero b-value acquisitions required for tensor estimation [25]. However, previous work in the brain investigating the dependence of DTI parameters on ND showed that higher ND reduced artifactually elevated FA [26,27] and its standard deviation (SD) [26], particularly in regions of low FA [28]. Higher SNR, as may be obtained by averaging, led to similarly lower and more accurate FA [29,30]. As a guide, $ND \geq 20$ was recommended for measurement of FA [26,31,32] while $ND \geq 30$ was suggested for measurement of tensor orientation and MD [26]. While the effects of ND and NR have been reported ex vivo [23], there have only been preliminary reports [33–36] that provide no conclusive evidence on the requirements of ND and NR for cDTI in vivo. A recent consensus statement on cDTI published by the Society for Cardiovascular Magnetic Resonance Cardiac Diffusion Special Interest Group recommended that more than six directions should be used but highlighted that rationalizing ND and NR remain an unmet need in the development of cDTI [1]. Furthermore, there exist various approaches for sampling low b-value data in cDTI. While there are methods for optimizing the quantity of low b-value data as a proportion of high b-value data in the brain [37], optimal sampling of low b-value data is less well understood in the heart.

In this study, we investigated the accuracy and precision of several diffusion sampling schemes over a wide range of ND and NR in healthy volunteers, extending our previous ex vivo work [23]. We compare time-normalized data to assess the trade-offs made between ND and NR, and examine the effects of the number of low b-value acquisitions. We hypothesized that accuracy and precision in DTI measurements would be improved by (i) sampling schemes that prioritize ND over NR, (ii) sufficient sampling of low b-value data, and (iii) longer scan times. This is intended to inform optimization and standardization of clinical cDTI protocols.

2. Methods

2.1. Data acquisition

cDTI data were acquired in healthy volunteers ($N = 10$) using a Prisma 3T magnetic resonance imaging (Siemens Healthineers, Erlangen, Germany) with maximum gradient amplitude, $Gmax = 80$ mT/m and a combination of 18-channel body and 32-channel spine radiofrequency array coils. The study was performed under approved ethics, and healthy volunteers provided written informed consent. Data were acquired with single-shot spin echo EPI, two-dimensional radiofrequency inner volume excitation and cardiac triggering: repetition time (TR) = 3 RR-intervals, TE = 76 ms, in-plane resolution = 2.3 ×

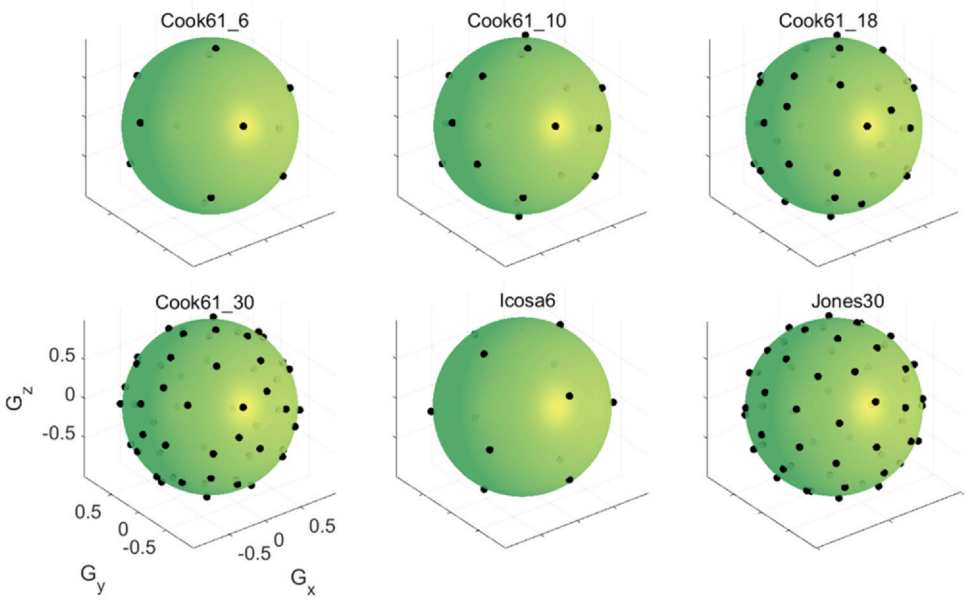

Fig. 1. Diffusion encoding schemes investigated include Cook61 diffusion encoding scheme subsampled to 6, 10, 18, and 30 directions, a 6-direction icosahedral scheme and a 30-direction scheme by Jones et al. Each direction was reflected on the opposite side of the sphere

2.3 mm ^{2}, slice thickness = 8 mm, number of slices = 3, field-of-view = 320 × 111 mm ^{2}, partial Fourier = 7/8, bandwidth = 2012 Hz/px, b_{low} = 50 and b_{high} = 500 s/mm^2. Up to second-order motion-compensated diffusion encoding gradient waveforms were applied. Subjects were scanned under free-breathing conditions without respiratory gating, in late systolic phase.

Diffusion-weighted data were acquired in pseudo-randomized fashion over a range of diffusion encoding schemes (DES) with different ND and NR. Low b-value data were acquired with ND = 3 orthogonal directions, denoted by $ND_{orth3,b50}$. High b-value data were acquired with a 61-direction Cook DES [38] that was sequentially subsampled to 6, 10, 18, and 30 direction sets. These DES were denoted as Cook61_6, Cook61_10, Cook61_18, and Cook61_30. The Cook DES was particularly amenable to subsampling because it was optimized for incremental sampling in case of premature scan termination. Previous work has shown that noise performance (and therefore the accuracy of parameter estimates) of a given DES is significantly correlated with the condition number of its transformation matrix [39]. Specific sets of sequentially subsampled directions were identified to minimize the condition numbers of the transformation matrices. This was performed by circularly subsampling ND = 6, 10, 18, and 30 sequential directions from the Cook61 scheme, incrementing the first diffusion encoding direction (D_i) from 1 to 61, and finding D_i that minimized the condition numbers. For the DES subsampled to 6, 10, 18, and 30 directions, condition numbers were relatively low at 1.74, 1.75, 1.70, and 1.58, respectively. For reference, the condition numbers of the widely used Jones30 and 6-direction dual gradient schemes are 1.59 and 2.00, respectively [39]. An icosahedral DES [40] with six diffusion encoding directions (Icosa6) and Jones DES [37] with 30 diffusion encoding directions (Jones30) were also acquired. An upper limit of 30 diffusion encoding directions was specified due to diminishing returns with higher ND [29]. These DES are illustrated in Fig. 1.

The full set of data acquired included $NR(ND_{orth3,\ b50})$ = 24, $NR(ND_{Cook61\_30,\ b500})$ = 12, $NR(ND_{Cook61\_6,\ b500})$ = 8, $NR(ND_{icosa6,\ b500})$ = 20, and $NR(ND_{Jones30,\ b500})$ = 4. This yielded a total number of acquisitions (NA_{all}) = 24 × 3 + 12 × 30 + 8 × 6 + 20 × 6 + 4 × 30 = 720 volumes, which constituted the reference dataset acquired in a single scan. The reference dataset was subsampled into the six DES listed in Fig. 1, with the total number of high b-value acquisitions (NA_{b500}) set to 30, 60, 90, and 120 volumes each. For a 6-direction scheme, this translated to NR = 5, 10, 15, and 20 repetitions, respectively. To keep acquisition times consistent, schemes with larger ND had proportionally lower NR. In cases where NA was not divisible by ND, e.g., Cook61_18, the last repetition of data would form an incomplete shell. Further to the DES, we also investigated the sensitivity of DTI to low b-value acquisitions. Here, we sampled the number of low b-value acquisitions (NA_{b50}) equal to a factor of the number of high b-value acquisition (NA_{b500}), where NA_{b50} = NA_{b500}/[10, 5, 3, 2]. For example, in a 6-direction scheme with NA_{b500} = 30, NA_{b50} = 3, 6, 10, and 15. The total number of acquisitions (NA_{all}) was the sum of NA_{b50} and NA_{b500}. This yielded 96 subsampled combinations, i.e., acquisition schemes comprising 6 DES, 4 sets of low b-value acquisitions, and 4 sets of high b-value acquisitions, as reflected in Table 1. The naming convention follows the format "DES_NA_{b500}_NA_{b50}," e.g., Cook61_30_90_30. Nominal acquisition time = NA_{all} × nominal TR = 720 × 3 s = 36 min, where nominal TR = number of slices × 60/heart rate, where data were acquired in a slice-interleaved manner and with assumed heart rate of 60 bpm.

2.2. Data analysis

Magnitude-only data were exported from the scanner and analyzed. Post-processing used in-house tools developed in Python. Image registration was performed by masking a suitable low b-value image using a square, registering all b_{low} images to this reference image, then using the average of registered b_{low} images as a reference image to register all images. The DTI signal representation was then fitted to the full dataset using robust weighted-least squares [41] implemented in DiPy [42], and the entire image series was predicted from this fit. All original images were then re-registered to these predicted images, leading to superior registration compared to the first stage. Rigid registration was performed using SimpleITK [43] with Mutual Information as a metric, calculated within the square mask. To assess the potential of signal rectification in the high b-value data, SNR_{b500} was calculated in a mid short-axis slice by taking the mean signal intensity over repetitions divided by the SD over repetitions [44] for each diffusion encoding direction in the registered data, and then averaging across directions and voxels.

Diffusion tensor fitting was performed on the registered images using robust weighted-least squares [41]. The robust fitting method has been previously shown to be superior to whole-image shot-rejection [41] and the weighted-least squares method mitigates signal

Table 1
Acquisition schemes extracted from the reference dataset, indicating numbers of diffusion encoding directions for high b-value data (ND_{b500}), numbers of acquisition volumes for high b-value data (NA_{b500}), number of repetitions for high b-value data (NR_{b500}), numbers of acquisition volumes for low b-value data (NA_{b50}), including three orthogonal diffusion encoding directions, total numbers of acquisition volumes (NA_{all}), and acquisition time.

Diffusion encoding scheme		Cook61_6/Icosa6				Cook61_10				Cook61_18				Cook61_30/Jones30			
ND_{b500}		6	6	6	6	10	10	10	10	18	18	18	18	30	30	30	30
NA_{b500}		30	60	90	120	30	60	90	120	30	60	90	120	30	60	90	120
NR_{b500}	= NA_{b500}/ND_{b500}	5	10	15	20	3	6	9	12	1.7	3.3	5	6.7	1	2	3	4
NA_{b50}	= NA_{b500}/[10, 5, 3, 2]	3	6	9	12	3	6	9	12	3	6	9	12	3	6	9	12
		6	12	18	24	6	12	18	24	6	12	18	24	6	12	18	24
		10	20	30	40	10	20	30	40	10	20	30	40	10	20	30	40
		15	30	45	60	15	30	45	60	15	30	45	60	15	30	45	60
NA_{all}	= NA_{b50} + NA_{b500}	33	66	99	132	33	66	99	132	33	66	99	132	**33**	**66**	**99**	**132**
		36	72	108	144	36	72	108	144	36	72	108	144	**36**	**72**	**108**	**144**
		40	*80*	*120*	*160*	*40*	*80*	*120*	*160*	*40*	*80*	*120*	*160*	***40***	***80***	***120***	***160***
		45	90	135	180	45	90	135	180	45	90	135	180	**45**	**90**	**135**	**180**
Time (s)	= N_{all} * 3RR intervals (= 3 s @ 60 bpm)	99	198	297	396	99	198	297	396	99	198	297	396	99	198	297	396
		108	216	324	432	108	216	324	432	108	216	324	432	108	216	324	432
		120	240	360	480	120	240	360	480	120	240	360	480	120	240	360	480
		135	270	405	540	135	270	405	540	135	270	405	540	135	270	405	540

For brevity and clarity, subsets of data with different diffusion encoding schemes (highlighted italics) and NAb50 (highlighted bold) are reported in detail in Section 3
NA number of acquisitions, *ND* number of diffusion encoding directions, *NR* number of repetitions

rectification bias in magnitude images [45]. cDTI parameters MD, FA, helix angle (HA), and sheetlet angle (E2A) were calculated. HA and E2A were measured using a cylindrical coordinate system with origin at the center of mass of the left ventricular (LV) segmentation on a slice-wise basis, as defined here [46]. Segmentation of the LV contours was performed with care taken to exclude voxels exhibiting partial-volume effects. Regions affected by strong artifacts that may negatively impact the results were masked out by defining "sectors" centered on the LV blood pool such that these voxels are ignored in the voxel statistics.

To assess the relative performance of each acquisition scheme, we use bootstrapping to approximate the sampling distribution of diffusion measures, by using the full reference dataset to generate samples of possible datasets that could be obtained from each acquisition scheme. Bootstrapping was done using the repetition bootknife method [47] which is a form of stratified bootstrapping. Each diffusion encoding direction was treated as a stratum, and each bootstrap sample was generated by randomly choosing (with replacement) images from each stratum, after first removing a random image from each stratum. A total of 500 bootstrap samples were generated per acquisition scheme (Table 1). This was well in excess of the minimum number of bootstrap samples required for stable measurements of accuracy and precision, and in a similar range as in the previous literature [48,49]. The number of images chosen from each stratum was based on the NR specified for each shell. Where NA_{b500} was perfectly divisible by ND_{b500}, i.e., in most cases, these images were distributed equally across diffusion encoding directions for the current shell. Where NA_{b500} was not perfectly divisible by ND_{b500} (e.g., in the Cook61_18 scheme with $NA_{b500} = 30$), any remaining images were then assigned to random unique directions within the design for the current shell, so there was at most a difference of 1 image per stratum in the current shell.

For each individual DES, accuracy was assessed by calculating the root mean squared difference (RMSD) between the bootstrap samples and the full reference dataset. Precision was assessed by the SD of cDTI metrics across bootstrap samples, whereby a lower SD reflected higher precision, i.e., precision $= (SD)^{-2}$. The mean, RMSD, and SD were then averaged over voxels in segmented regions-of-interest in a mid-myocardial slice and in the mid-ventricular septal wall, i.e., American Heart Association regions 8 and 9, to exclude regions with poorer B_0 homogeneity, e.g., near the posterior vein. Boxplots of mean, RMSD, and SD are presented with median and interquartile range (IQR) over subjects. Individual bootstrap sample data in all volunteers from selected DES were also presented as histograms. The data were fitted using normal distributions. Non-overlapping 95% confidence intervals (CI) of the mean indicate statistically significant differences between acquisition schemes. Paired t-tests for RMSD and SD measures were performed between each acquisition scheme. P-values were adjusted for multiple comparisons using Bonferroni-Holm correction [50] with a significance threshold of $p < 0.05$. P-value matrices were calculated, and cDTI parameters compared against nominal imaging time.

3. Results

Subject characteristics were age = 23 ± 4 years, 1 male, 9 females, average heart rate = 71 ± 10 beats per minute (bpm), weight = 61 ±

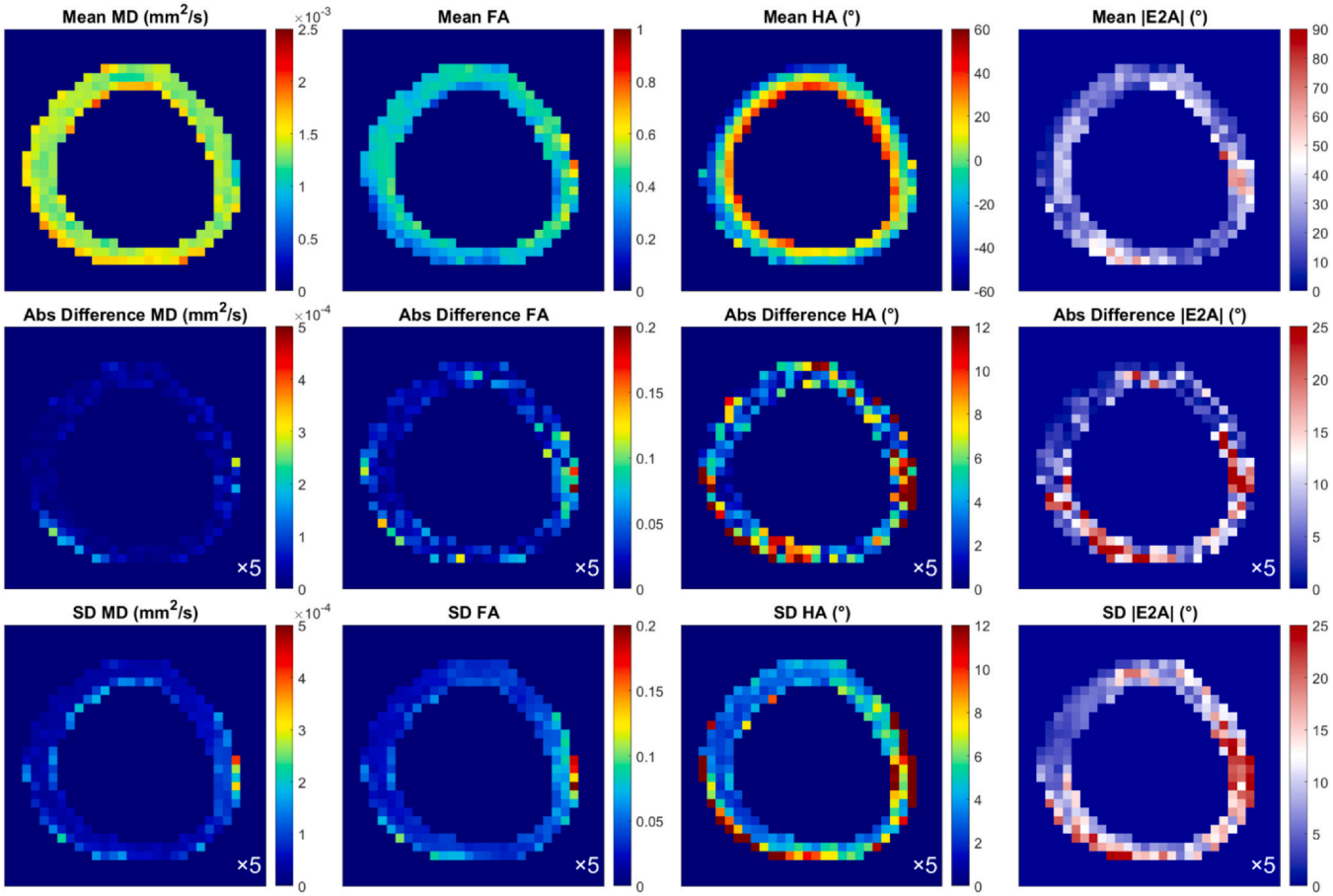

Fig. 2. cDTI maps MD, FA, HA, and |E2A| in *a* mid-myocardial short-axis slice in *a* representative healthy volunteer using the example diffusion encoding scheme Cook61_30 with $NA_{b500} = 90$ and $NA_{b500} = 30$. (Top) Mean over bootstrap samples, (middle) absolute difference between current and reference diffusion encoding scheme, and (bottom) standard deviation across bootstrap samples. Region of elevated absolute difference and SD in the inferolateral wall is indicated by arrows. These maps were scaled at 5× smaller range to highlight the heterogeneity. *cDTI* cardiac diffusion tensor imaging, *MD* mean diffusivity, *FA* fractional anisotropy, *HA* helix angle, *|E2A|* absolute sheetlet angle, *NA* number of acquisitions, *SD* standard deviation

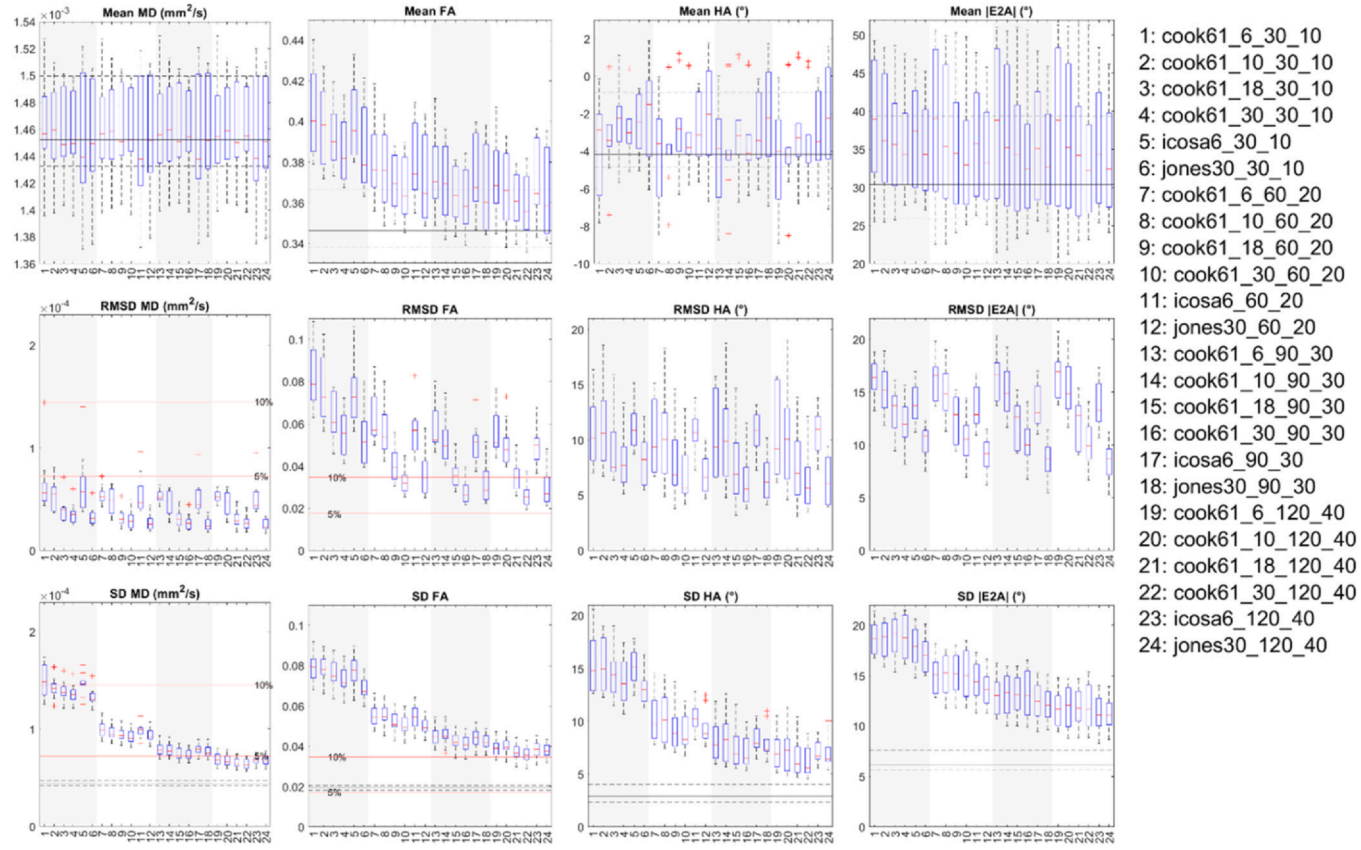

Fig. 3. Boxplots of cDTI metrics (left to right) MD, FA, HA, and |E2A| showing (top) cDTI metrics averaged over bootstrap samples, (middle) RMSD with respect to the fully sampled reference data, and (bottom) SD across bootstrap samples across a mid-myocardial short-axis slice. Twenty-four acquisition schemes are described in the following format "DES_NA_{b500}_NA_{b50}," e.g., Cook61_30_90_30. These were sorted by diffusion encoding scheme and grouped into four groups (white and gray vertical bands) with increasing NA_{all} corresponding to increasing acquisition times. For reference, median and IQR values from the reference dataset are given (black solid and dashed lines); 5% and 10% of the median MD and FA from the reference dataset are indicated (red solid lines). *cDTI* cardiac diffusion tensor imaging, *MD* mean diffusivity, *FA* fractional anisotropy, *HA* helix angle, *|E2A|* absolute sheetlet angle, *RMSD* root mean squared difference, *NA* number of acquisitions, *SD* standard deviation, *DES* diffusion encoding schemes, *IQR* interquartile range

10 kg, and body mass index = 22 ± 2 (mean ± SD across subjects). SNR_{b500} was 9.6 ± 1.0 (mean ± SD across subjects). An example of image quality and registration performance is given (Supplementary Video 1).

Supplementary material related to this article can be found online at doi:10.1016/j.jocmr.2025.101951.

MD, FA, HA, and |E2A| maps in a representative volunteer are shown (Fig. 2). The maps are consistent with those reported in the literature. Absolute differences with respect to the reference data and SD were elevated in the inferolateral wall, corresponding to the region near the posterior vein, but this effect was less distinct in the average parameter maps.

Boxplots reflecting (i) cDTI metrics averaged over bootstrap samples, (ii) accuracy of cDTI metrics expressed as the RMSD with respect to the fully sampled reference data, and (iii) 1/sqrt(precision) as expressed by SD across bootstrap samples across a mid-myocardial short-axis slice are shown (Fig. 3; median and IQR over subjects). For clarity of presentation, we focused first on 24 acquisition schemes with 6 different DES and 4 different total acquisition times. In all cases, NA_{b500}:NA_{b50} = 3. For context, these schemes are highlighted in yellow in Table 1. In the reference data, mean MD = (1.46 ± 0.04) × 10^{-3} mm^2/s, mean FA = 0.35 ± 0.02, mean HA = −3.4° ± 3.0°, mean |E2A| = 32.9° ± 10.0° (mean ± SD across subjects). Within each band with normalized acquisition times in Table 1, there was a small but observable trend toward lower RMSD and SD in MD, FA, HA, and |E2A| with higher ND, indicating higher accuracy and precision. This was consistent across Cook, Icosa, and Jones DES. For the same acquisition time, for the ND = 30 schemes (Cook and Jones), RMSD MD, FA, HA, and |E2A| were on average 48%, 40%, 34%, and 34% lower than for the ND = 6 schemes (Cook and icosahedral). Similarly, SD of MD, FA, HA, and |E2A| were 6.8%, 7.8%, 10%, and 1% lower in the former compared to the latter. Mean FA was most sensitive to DES, while MD, HA, and |E2A| were less so.

Across bands with different acquisition times, there was a clear trend toward lower SD (i.e., better precision) in all cDTI metrics with increasing number of acquisitions and scan time. For ease of reference, these results were reformatted into bands with different DES and ordered by increasing NA_{all} within each band (Supplementary Fig. 2-4). For completeness, mean E2A is reported (Supplementary Fig. 4), with mean E2A = 1.7° ± 7.1°.

A subset of 6 acquisition schemes corresponding to NA_{all} = NA_{b500} + NA_{b50} = 120 are presented as histograms (Fig. 4). RMSD and SD for MD, FA, HA, and |E2A| were significantly lower for ND ≥ 18 compared to ND = 6 data, indicating better accuracy and precision in DES with greater number of directions rather than repetitions. This applied across Cook, icosahedral, and Jones diffusion schemes. P-value matrices illustrate significant differences ($p < 0.05$) between acquisition schemes, which were most prominent in precision (SD) and least prominent in mean values across different ND and NA (Fig. 5).

We also report the mean, RMSD, and SD for the four cDTI parameters as a function of numbers of low and high b-value acquisitions, NA_{b50}, and NA_{b500}. For clarity, only a single DES Cook61_30 is presented (Fig. 6). For context, these schemes are highlighted in bold in Table 1. Within each band of fixed NA_{b500}, there was a trend

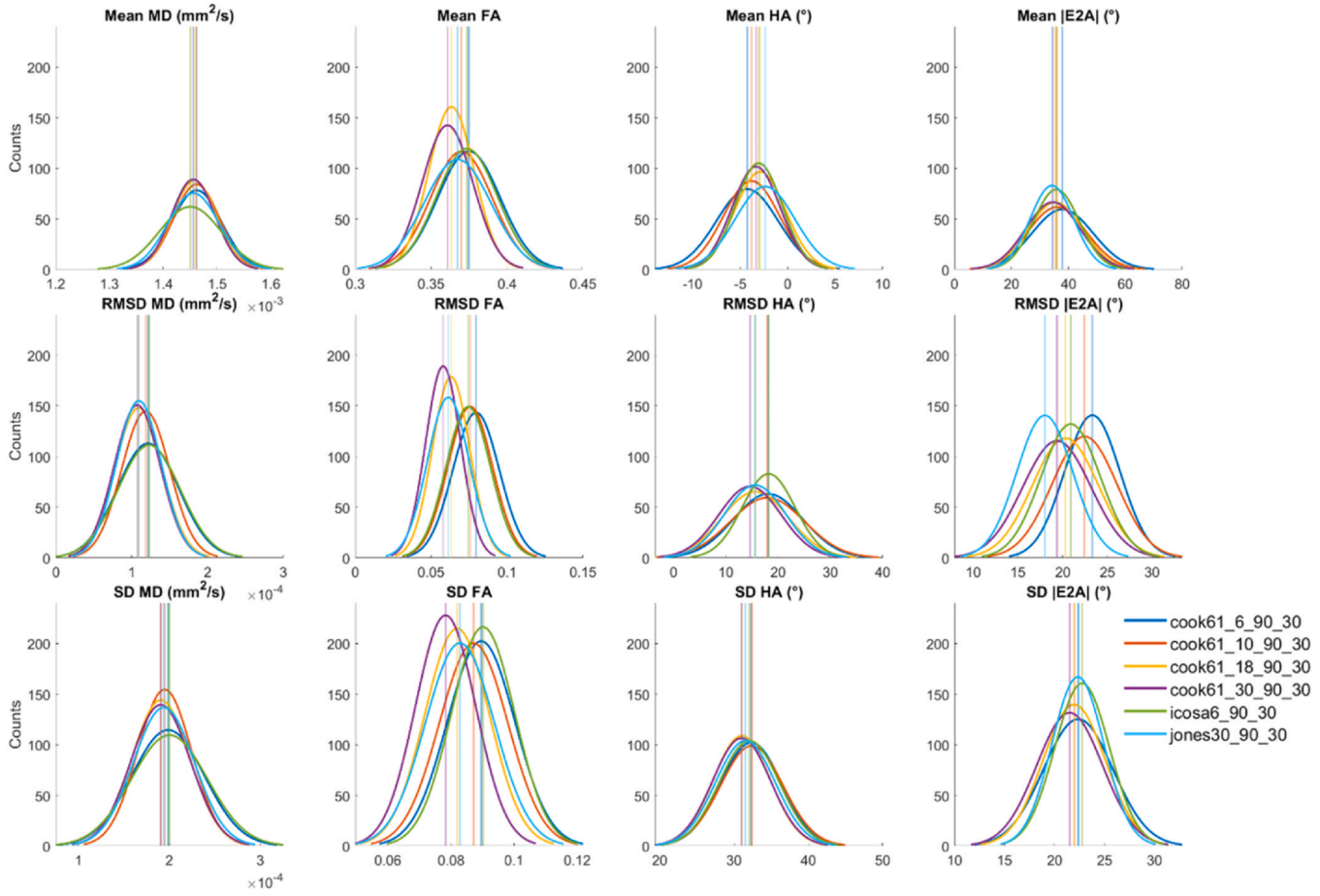

Fig. 4. Histograms of (top to bottom) mean, RMSD, and SD of (left to right) MD, FA, HA, and |E2A| across 500 bootstrap samples and healthy volunteers (N = 10). Data from six time-normalized acquisition schemes are presented, with vertical lines indicating 95% confidence intervals of the mean. Non-overlapping 95% CI indicate significant differences between groups. *MD* mean diffusivity, *FA* fractional anisotropy, *HA* helix angle, *|E2A|* absolute sheetlet angle, *RMSD* root mean squared difference, *SD* standard deviation, *CI* confidence intervals

toward lower RMSD and SD of MD and FA. A similar trend was observed in RMSD and SD of HA and |E2A| at lower total number of acquisitions ($NA_{all} < 45$), but was not discernible at higher NA_{all}. For the same NA_{b500}, the schemes with NA_{b500}:$NA_{b50} = 2$ had on average, RMSD MD, and FA that were 29% and 13% lower than the NA_{b500}:$NA_{b50} = 10$ schemes. Similarly, SD MD and FA were 46% and 20% lower in the former compared to the latter.

A subset of a single DES with four sets of NA_{b50} are presented as histograms (Fig. 7). RMSD and SD of MD and FA were significantly lower for $NA_{b50} \geq 18$ compared to $NA_{b50} \leq 10$ data, indicating better accuracy and precision with greater number of low b-value acquisitions. No significant differences were observed in RMSD and SD of HA and |E2A|. P-value matrices illustrate significant differences ($p < 0.05$) that were most prominent in accuracy (RMSD) and precision (SD) of MD and FA across different NA_{b50} and NA_{all} (Fig. 8).

Data in the mid-ventricular septal wall are presented (Supplementary Figs. 5 and 6). Notwithstanding the larger error bars due to fewer voxels, similar trends were observed as compared to the whole mid-ventricular slice data. This suggests that structured noise in regions more greatly affected by susceptibility effects, i.e., near the posterior vein, did not detract from the overall findings.

Average mean, RMSD, and SD of cDTI parameters were evaluated as a function of acquisition time (Fig. 9). The data show decreasing RMSD and SD with increasing NA_{all} and scan time. The majority of DES investigated yielded an RMSD MD of < 5% and SD MD of < 10% of the reference MD. Acquisition schemes DES_{All}_90_45, DES_{All}_120_40, and DES_{All}_120_60 yielded SD MD of < 5% of the reference MD, where DES_{All} corresponded to all DES. Differences in MD between time-normalized DES were marginal. DES were ranked from most to least accurate FA (i.e., lowest to highest RMSD): Cook61_30, Jones30, Cook61_18, Icosa6, Cook61_10, Cook61_6, with RMSD FA < 10% of the reference FA for Cook61_30/Jones30 with $NA_{all} \geq 108$. SD FA < 10% of the reference FA for Cook61_30_120_60 only. DES were ranked (i) from most to least accurate HA: Cook61_30, Jones30, Cook61_18, Cook61_10, Cook61_6, Icosa6, (ii) from most to least precise HA: Cook61_30, Cook61_18, Jones30, Icosa6, Cook61_10, Cook61_6, (iii) from most to least accurate |E2A|: Jones30, Cook61_30, Cook61_18, Icosa6, Cook61_10, Cook61_6, and (iv) from most to least precise |E2A|: Jones30, Icosa6, Cook61_10, Cook61_6, Cook61_18, Cook61_30. $NA_{b500} = 120$ and Cook61_30/Cook61_18 was needed to achieve SD HA < 7°, while SD |E2A| < 13° was achievable with $NA_{b500} = 120$ and Jones30, Icosa6.

Higher NA_{all}, i.e., longer acquisition times led to improved precision in all DTI metrics whereby quadrupling NA_{all} from 40 to 160 volumes led to *a* 53%, 50%, 53%, and 36% reduction in SD in MD, FA, HA, and |E2A|, averaged across 6 DES. In relative terms, this corresponded to *a* reduction in SD MD from 9.7% to 4.6% and SD FA from 22% to 11%, expressed as *a* percentage of the mean MD and FA of the reference data. Similarly, accuracy improved with *a* 20%, 39%, 11%, and 5.4% reduction in RMSD in MD, FA, HA, and |E2A| from 40 to 160 acquired volumes. In relative terms, this corresponded to a reduction in RMSD MD from 3.3% to 2.7% and RMSD FA from 19% to 12% of the reference mean MD and FA. RMSD and SD in selected acquisition schemes are given in Table 2.

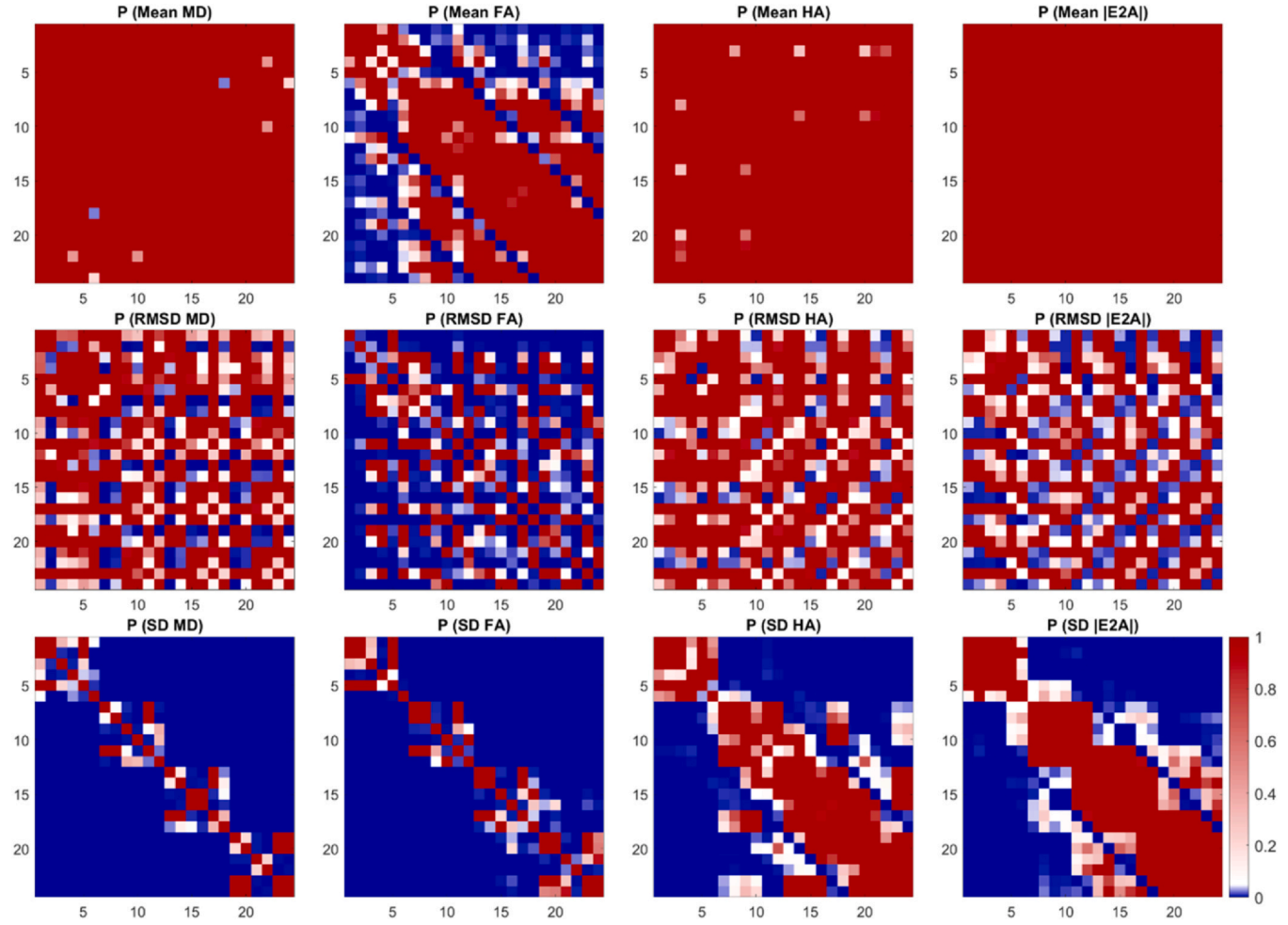

Fig. 5. P-value matrices reflecting pairwise comparisons between the 24 acquisition schemes given in Fig. 3 with $p < 0.05$ (blue), $p = 0.05$ (white), and $p > 0.05$ (red). *MD* mean diffusivity, *FA* fractional anisotropy, *HA* helix angle, *|E2A|* absolute sheetlet angle, *RMSD* root mean squared difference, *SD* standard deviation

4. Discussion

We evaluated 96 acquisition schemes in terms of accuracy and precision with respect to the 720 volumes, i.e., ~36-minute reference datasets. First, we observed that accuracy and precision in all estimates improved with NA_{all} and acquisition time, consistent with previous reports [23,35]. Second, we found that prioritizing ND over NR given a fixed acquisition time improved accuracy and precision in general. Differences in accuracy and precision between different DES with equal ND and NA_{all} were less prominent and generally not significant.

In our pilot work in healthy volunteers [35], we reported RMSD MD = 2.29 ($\times 10^{-4}$ mm^2/s), RMSD FA = 0.08, and RMSD HA = 13° using a Jones scheme with ND = 6, NA_{b50} = 24, and NA_{b500} = 96. The accuracy improved to RMSD MD = 1.11 ($\times 10^{-4}$ mm^2/s), RMSD FA = 0.04, and RMSD HA = 7.8° when using a Caruyer scheme [51] with a larger number of directions, i.e., ND = 96 and NR = 1. It was concluded that precision in cDTI was improved by prioritizing ND over NR for a given acquisition time. This was supported by more recent work evaluating $6 \leq ND \leq 30$, where it was reported that increasing ND led to reduced RMSD in cDTI parameters, and that recommended an experimental design strategy that maximizes ND [36]. In the current study, the nearest equivalent acquisition scheme to the former was Cook61_6_90_30 which yielded RMSD MD = 0.794 $\times$ 10^{-4} mm^2/s, RMSD FA = 0.04, and RMSD HA = 8.4°. This represented an improvement in accuracy compared to the previous study, which may be attributed to the improved post-processing pipeline with robust fitting of tensors [52] over shot rejection. Direct comparison to a 96-direction DES was not available. Another pilot study in healthy volunteers (N = 5) explored time-normalized cDTI acquisitions with six DES where ND = 6, 10, 12, 15, 20, 30 and NR = 10, 6, 5, 4, 3, 2, respectively [34]. The authors reported minimal differences in median and interquartile intervals of MD and FA, and they suggested that the acquisition scheme was not critical to measuring MD and FA. In a separate study using stimulated echo acquisition mode (STEAM), no significant differences were found in MD and FA between time-normalized averaged datasets where ND = 6, 10, 12, and 20 [53]. Our results suggest otherwise and indicate that prioritizing ND over NR for a given scan time, up to ND = 30, improves accuracy and precision of cDTI parameters. For example, RMSD and SD in MD and FA were significantly lower in Cook61_30_120_40 compared to Cook61_6_120_40 ($p < 0.001$). Moreover, there is potential for poor image quality associated with specific diffusion encoding directions due to eddy current effects. Acquiring the minimum of ND = 6 provides no redundancy in case a specific diffusion encoding direction gives rise to sub-optimal image quality.

The effects of ND have also been reported ex vivo [23,54]. One study in fixed pig hearts found that reliable estimation of HA could be obtained with ND/NR = 12/6, 30/3, or 64/2, recommending the 12/6 combination as one with the shortest (< 10 min) acquisition time [54]. However, only qualitative assessments were reported and data were not time-normalized. A second study in fixed rat hearts investigated the effects of ND, SNR, and spatial resolution on the accuracy and precision of cDTI [23]. It was shown that for a given scan time, the precision of

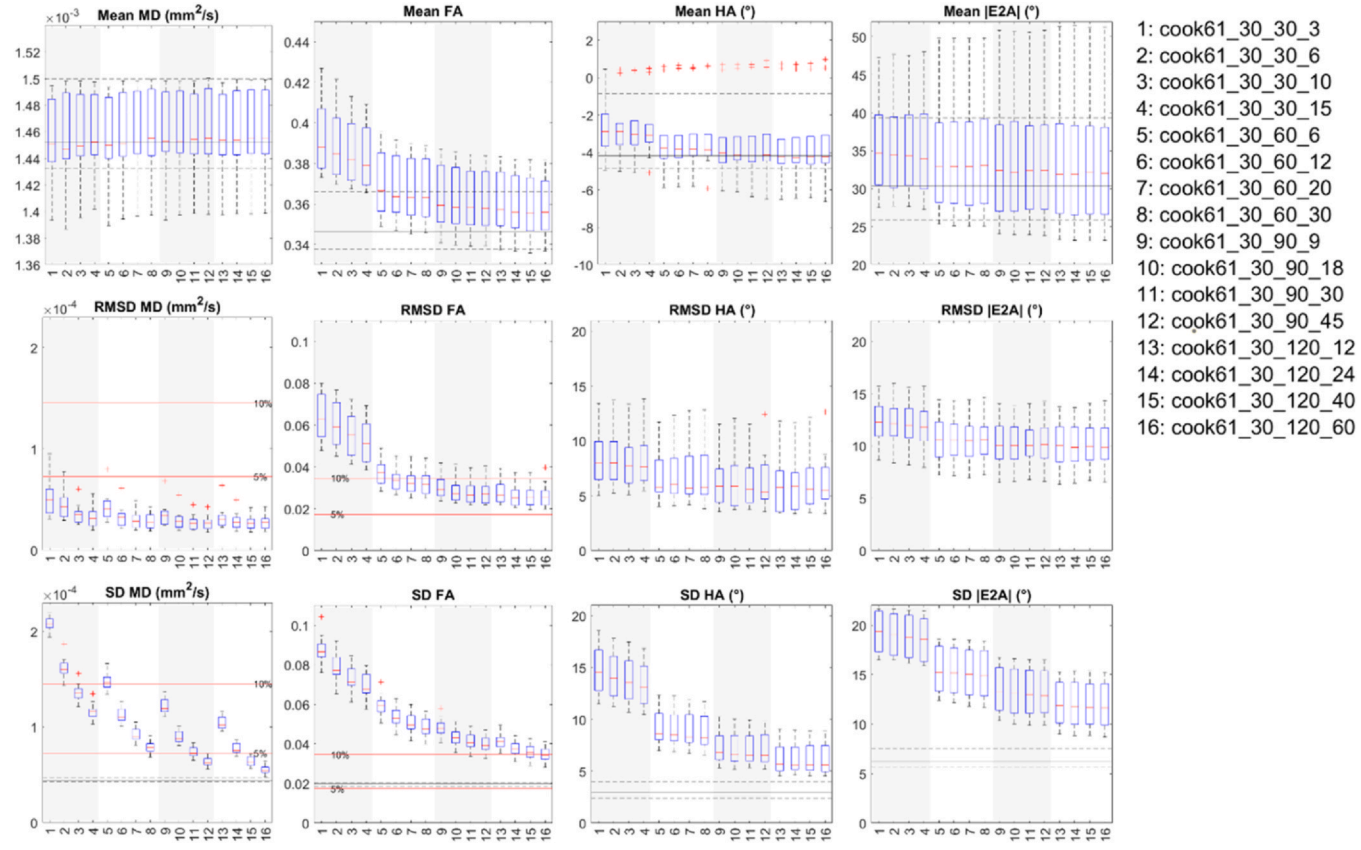

Fig. 6. Boxplots of cDTI metrics (left to right) MD, FA, HA, and |E2A| showing (top) cDTI metrics averaged over bootstrap samples, (middle) RMSD with respect to the fully sampled reference data, and (bottom) SD across bootstrap samples across a mid-myocardial short-axis slice. Sixteen acquisition schemes were sorted by number of low b-value acquisitions (NA_{b50}) and grouped into four groups (white and gray vertical bands) with increasing NA_{all} corresponding to increasing acquisition times. For reference, median and IQR values from the reference dataset are given (black solid and dashed lines); 5% and 10% of the median MD and FA from the reference dataset are indicated (red solid lines). *cDTI* cardiac diffusion tensor imaging, *MD* mean diffusivity, *FA* fractional anisotropy, *HA* helix angle, *|E2A|* absolute sheetlet angle, *RMSD* root mean squared difference, *SD* standard deviation, *NA* number of acquisitions

FA, HA, |E2A|, transverse angle, sheetlet elevation, and sheetlet azimuth for *a* given scan time were largely independent of the choice of increasing NR or ND, on the assumption that SNR is proportional to √NR. In practice, physiological effects in vivo, such as residual motion effects arising from breathing and cardiac contraction, contribute *a* significant additional noise-like component that violates the above assumption, resulting in spatially correlated variations in parameters. This may, to an extent, reduce the value of additional NR and support our current findings of prioritizing ND over NR, up to ND = 30. Extrapolating to typical parameter settings, e.g., resolution used in the clinic, the study suggested that the expected bias in MD and FA were 2.1% and 13% and precision in MD and FA were ± 4.9% and ± 30% with respect to the ground truth; precision of HA and |E2A| were ± 14°and ± 24°, respectively. This compares well with our current findings of bias in MD and FA of 2.7% and 12% and precision in MD and FA of 4.6% and 11% for an NA = 160 dataset with respect to the reference data, noting that the previous study reported precision over voxels rather than bootstrap samples. Direct comparisons between ex vivo and in vivo data are difficult due to various reasons, such as different physiological status and temperature of the myocardium. Nonetheless, our current findings similarly reflect that precision of MD is superior to that of FA, and precision of HA is superior to that of |E2A|, although the specific values differ. While *a* ground truth does not exist in vivo, we can see that the trends in accuracy and precision appear to approach an asymptotic value by NA_{all} = 160, justifying the appropriateness of NA_{all} = 720 as suitable reference data.

In the above rat heart study, precision in MD was optimized by maximizing NR of non-diffusion-weighted scans at the expense of ND, for *a* given scan time. This leads us to our third observation that accuracy and precision of MD, and to *a* lesser extent FA, improved with increasing numbers of low *b*-value acquisitions NA_{b50}, with disproportionately large benefits at low NA_{all}. With larger $NA_{all} \geq 99$, as more commonly used in the clinic, improvements in both accuracy and precision in MD and FA were retained. For example, with DES Cook61_30, NA_{b500} = 90 and NA_{b50} = [9, 18, 30, 45], the improvements in precision of MD and FA between each increasing step of NA_{b50} were significant ($p < 0.001$). Accuracy in MD improved when NA_{b50} increased from 9 to 18 ($p < 0.05$), but was not significantly better between successive increments of higher NA_{b50}.

Other studies investigated the sensitivity of cDTI to SNR in human hearts [49] and in fixed rat hearts [55]. In the former, systolic median 95% CI of the first, second, and third eigenvectors ($\mathbf{v_1}$, $\mathbf{v_2}$, and $\mathbf{v_3}$) were 15.5°, 31.2°, and 21.8°. The authors concluded that precision improved with increasing SNR, but the improvements were minimal beyond NR = 10 corresponding to a 10-min scan. This was consistent with our findings. The latter study reported that mean 95%CI of $\mathbf{v_1}$, $\mathbf{v_2}$, and $\mathbf{v_3}$ was 3.7°, 10.9°, and 10.6°, respectively. The poorer precision in vivo may reflect the additional challenges of motion and lower spatial resolution in vivo. While higher image resolution in vivo is desirable to minimize partial-volume effects, this is generally limited by SNR, and we employed a moderate image resolution of 2.3 × 2.3 × 8 mm^3 to maximize generalizability.

Precision and bias of cDTI measurements could potentially be affected by several factors. These include orientation and anisotropy of the underlying diffusion tensor [27], physiological "noise" due to residual cardiac and respiratory motion effects, and signal rectification

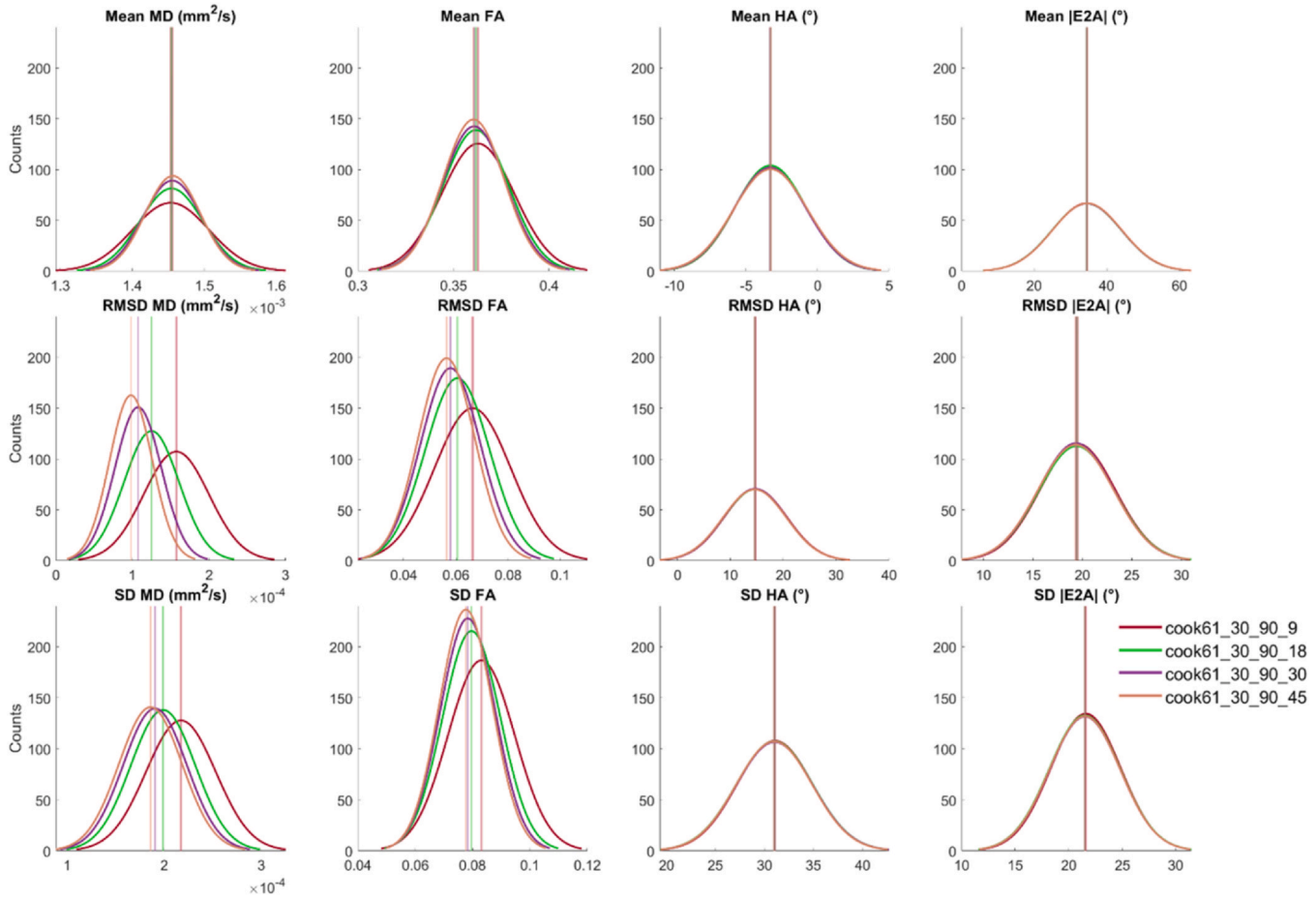

Fig. 7. Histograms of (top to bottom) mean, RMSD and SD of (left to right) MD, FA, HA, and |E2A| across 500 bootstrap samples and healthy volunteers (N = 10). Data from a single diffusion encoding scheme with different numbers of low b-value acquisitions (NA_{b50} = 9, 18, 30, 45) are presented, with vertical lines indicating 95% confidence intervals of the mean. Non-overlapping 95% CI indicate significant differences between groups. *MD* mean diffusivity, *FA* fractional anisotropy, *HA* helix angle, *|E2A|* absolute sheetlet angle, *RMSD* root mean squared difference, *SD* standard deviation, *NA* number of acquisitions, *CI* confidence intervals

due to insufficient SNR. Signal rectification can be mitigated by using weighted squares fitting, as well as complex image data reconstruction [22,56–58]. However, these do not resolve the contribution of physiological "noise" which can be substantial.

The recommended protocols for cDTI will depend on several factors, including the precision of the measurement, the expected differences, e.g., between health and pathology, the parameters of interest, subject compliance, and scan time available. Despite our finding that higher NA_{all} improved precision, this improvement comes with diminishing returns at higher NA_{all}. Moreover, longer scans, e.g., > 10 min, can be challenging to perform in a clinical setting due to limited scan times and increased likelihood of patient discomfort leading to greater patient motion, poorer image quality, and premature termination of scans. For context, we consider the range of cDTI parameters seen in clinical cohorts. Where the differences between health and disease are known and expected to be small, the acquisition would need to be designed with greater precision. In general, studies report higher MD and lower FA in disease cohorts relative to controls. In a study of patients post-myocardial infarction [2], MD was 14% higher, FA was 31% lower, and HA was between −7° and +5° relative to controls. In patients with hypertrophic cardiomyopathy [7,8,10,11], MD was between 2% and 10% higher, FA was between 6% and 17% lower relative to controls. Patients with amyloidosis had 26% higher MD and 29% lower FA relative to controls [13]. Similarly, patients with aortic stenosis had 6% higher MD and 17% lower FA relative to controls [12]. HA and E2A differences in pathology have been primarily reported in terms of HA slope or |E2A| [2,7,8,10,12,59] and differences in HA may not be directly comparable. Other studies that reported |E2A| were based on STEAM [3,9], which is known to yield substantially different measurements compared to spin echo. We additionally reported E2A instead of |E2A| to avoid loss of signed information that reflects on sheetlet orientation (Supplementary Fig. 4). This is particularly useful in assessing bias across different regions with positive and negative E2A. Averaging across the myocardium means that regions with positive and negative E2A cancel out resulting in mean E2A < mean |E2A|.

To achieve SD MD of < 5% of the reference mean, $NA_{b50} \geq 45$ with any DES was required. This included DES_{All}_90_45, DES_{All}_120_40, and DES_{All}_120_60 where DES_{All} refers to any of six DES evaluated. DES_{All}_90_45 had the shortest acquisition time of 6:45 min. In contrast, only Cook61_30_120_60 yielded SD FA of < 10% of the reference, i.e., 9.8%, corresponding to an acquisition time of 9:00 min. Other sequences, e.g., Cook61_30_120_40, came close with SD FA = 10.2% with an acquisition time of 8:00 min. That SD FA > SD MD was consistent with the greater sensitivity of FA to noise. SD HA and SD |E2A| were more sensitive to NA_{all} and DES, and less so to NA_{b50}. Besides extending the acquisition time, precision in HA and |E2A| could be improved by prioritizing ND over NR, e.g., ND = 30, gave higher precision than ND = 6, given the same total acquisition time. For clinically relevant protocols, our findings support the use of ND = 30. We would also recommend NA_{b50}:$NA_{b500} \geq 1/3$ for better precision in MD and FA. If only MD were desired, *a* shorter protocol of < 7 min would be reasonable. We would recommend protocols of > 8 min to obtain good precision for FA, HA, and |E2A|, subject to availability of scan time.

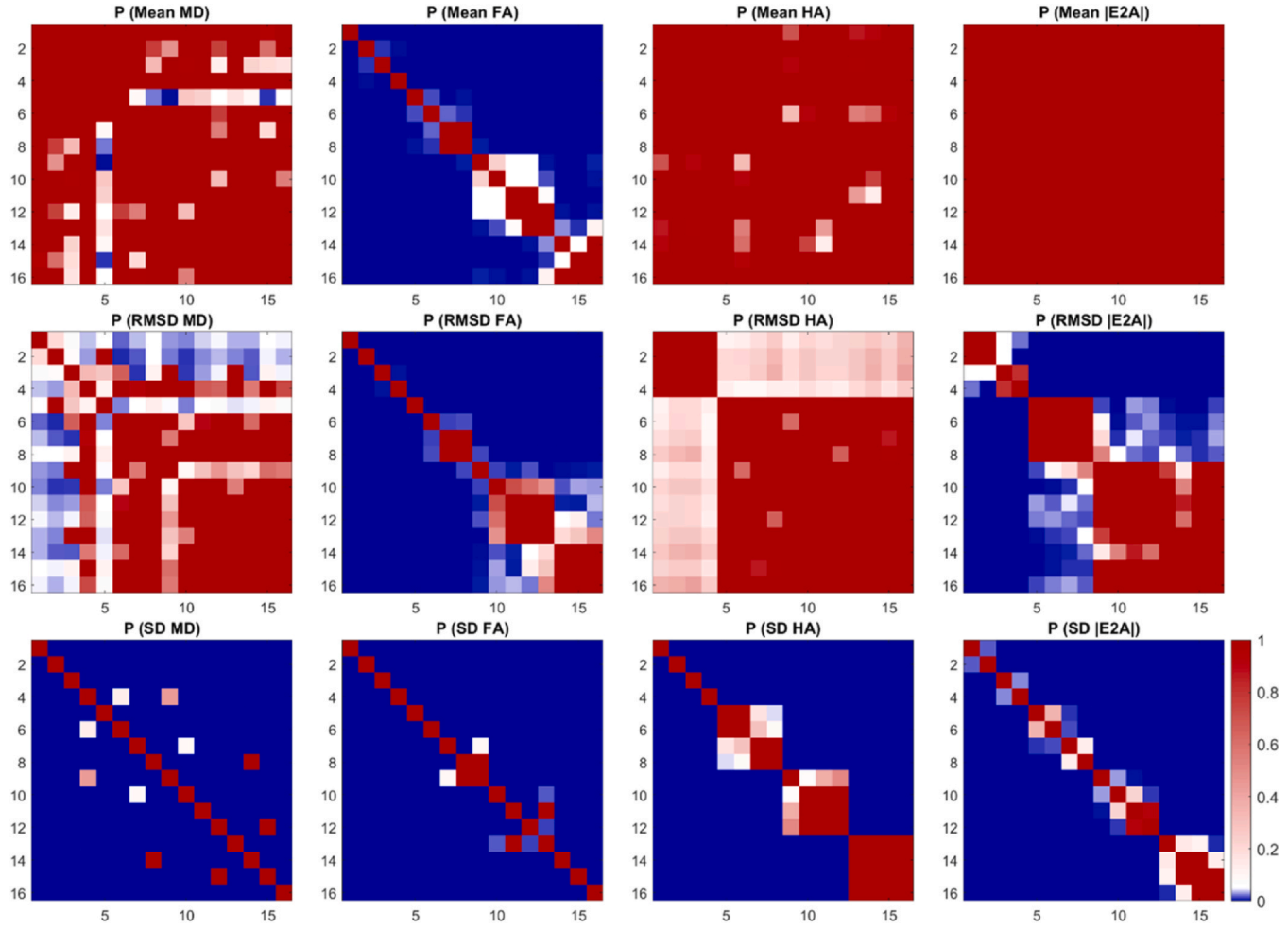

Fig. 8. P-value matrices reflecting pairwise comparisons between the 16 acquisition schemes given in Fig. 6 with $p < 0.05$ (blue), $p = 0.05$ (white), and $p > 0.05$ (red). *MD* mean diffusivity, *FA* fractional anisotropy, *HA* helix angle, *|E2A|* absolute sheetlet angle, *RMSD* root mean squared difference, *SD* standard deviation

5. Limitations

In this study, we have only considered healthy volunteers with good compliance over the entire ~36 min scan, excluding setup and planning. It is foreseeable that some patients will have poorer compliance leading to poorer image quality, accuracy, and precision, suggesting more acquisition volumes and time would be needed to achieve similar levels of accuracy and precision. However, longer acquisition times are likely to contribute to worse compliance and may be infeasible. In the ideal case, we would examine accuracy and precision in a similar study in patients. In practice, such efforts may need to be combined with techniques for accelerating image acquisition, such as simultaneous multi-slice imaging [60], compressed sensing [61,62], and deep learning [63–66].

Image distortion remains a common issue in cDTI. This stems mostly from the use of single-shot EPI readouts and consequent sensitivity to susceptibility-induced distortion. This commonly manifests as artifactual compression or dilation of the myocardium, especially near the posterior vein. In this study, we have seen that this effect also contributes to reduced local accuracy and precision. Recent developments in distortion correction using reversed phase encoding data for correction of susceptibility artifacts promise to improve the geometric fidelity of the images [67]. Distortions can also be caused by eddy current effects and can be an issue particularly in M2SE cDTI where large diffusion encoding gradients are used [22]. Methods based on gradient impulse response functions and diffusion gradient response functions [68] and potentially gradient system transfer functions [69] can be an effective tool in correcting for eddy current effects.

In this study, we used a free-breathing approach without respiratory navigators and/or slice tracking. This suggests that the data would have been susceptible to through-slice motion, which we estimate to within ± 1.5 mm. This was mitigated through the use of robust fitting to exclude outliers [41], the use of thick 8 mm slices, and acquisition of multiple diffusion encoding directions and repetitions, yielding high-quality DTI maps. While some studies have adopted approaches for managing through-slice motion, e.g., breath-holding [22], respiratory navigators [14,70], and/or slice tracking [19], these techniques either reduce scan efficiency and/or rely on assumptions of heart geometry and motion, and are an incomplete solution. Compensation for respiratory motion in cDTI remains an area of ongoing development. Furthermore, M2SE cDTI is sensitive to cardiac phase [49], and this study focused on imaging in late systole when the acquisition is most robust.

To maximize the number and scope of acquisition schemes compared, we relied partially on subsampling of the modified Cook61 DES. This meant that (i) the subsampled data were not fully independent of each other, and (ii) the distribution of diffusion encoding directions in subsampled schemes was not fully optimal. To mitigate these, fully optimized Icoas6 and Jones30 schemes were employed as independent controls. Their accuracy and precision

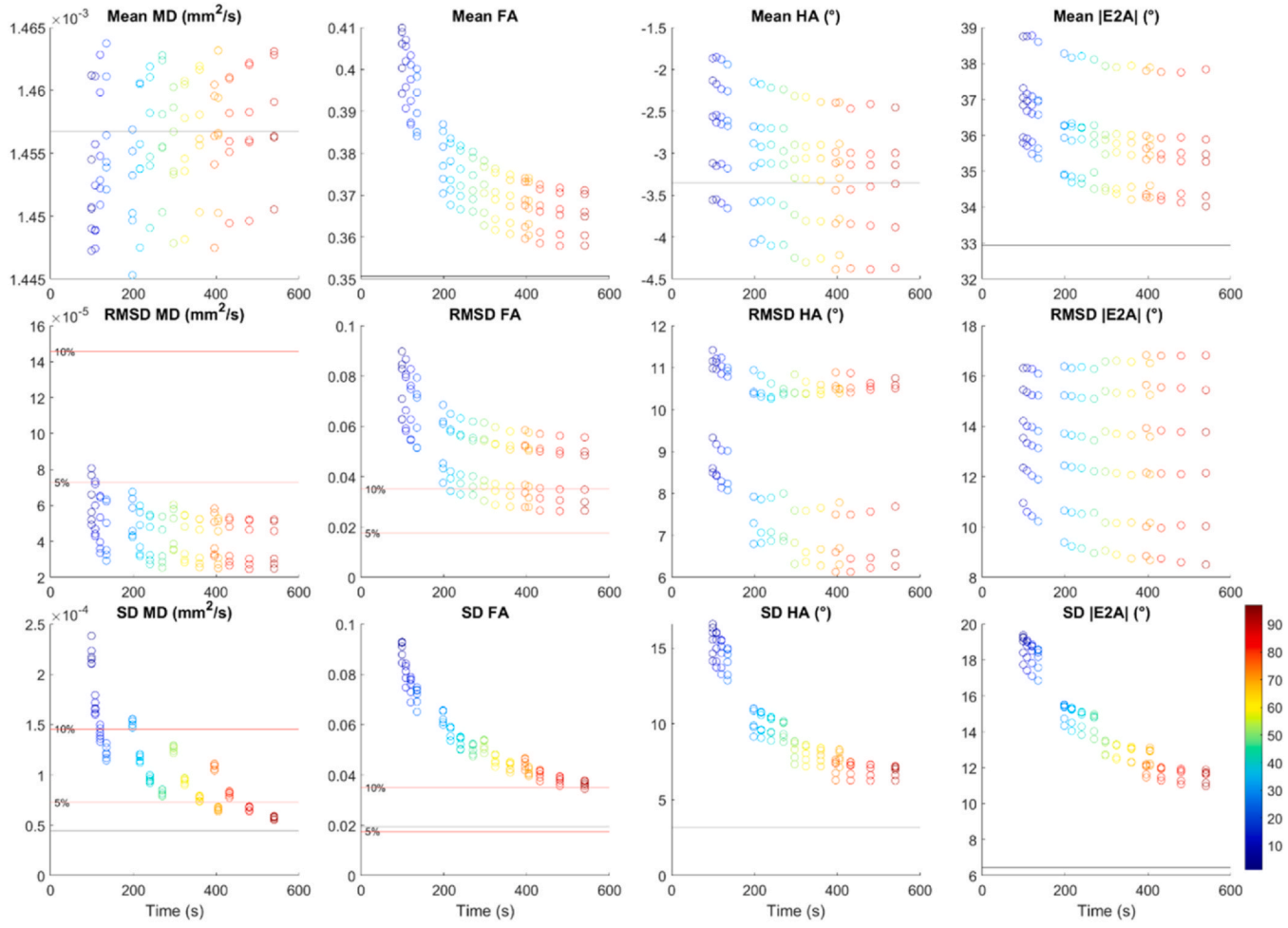

1: cook61_6_30_3
2: cook61_10_30_3
3: cook61_18_30_3
4: cook61_30_30_3
5: icosa6_30_3
6: jones30_30_3
7: cook61_6_30_6
8: cook61_10_30_6
9: cook61_18_30_6
10: cook61_30_30_6
11: icosa6_30_6
12: jones30_30_6
13: cook61_6_30_10
14: cook61_10_30_10
15: cook61_18_30_10
16: cook61_30_30_10
17: icosa6_30_10
18: jones30_30_10
19: cook61_6_30_15
20: cook61_10_30_15
21: cook61_18_30_15
22: cook61_30_30_15
23: icosa6_30_15
24: jones30_30_15
25: cook61_6_60_6
26: cook61_10_60_6
27: cook61_18_60_6
28: cook61_30_60_6
29: icosa6_60_6
30: jones30_60_6
31: cook61_6_60_12
32: cook61_10_60_12
33: cook61_18_60_12
34: cook61_30_60_12
35: icosa6_60_12
36: jones30_60_12
37: cook61_6_60_20
38: cook61_10_60_20
39: cook61_18_60_20
40: cook61_30_60_20
41: icosa6_60_20
42: jones30_60_20
43: cook61_6_60_30
44: cook61_10_60_30
45: cook61_18_60_30
46: cook61_30_60_30
47: icosa6_60_30
48: jones30_60_30
49: cook61_6_90_9
50: cook61_10_90_9
51: cook61_18_90_9
52: cook61_30_90_9
53: icosa6_90_9
54: jones30_90_9
55: cook61_6_90_18
56: cook61_10_90_18
57: cook61_18_90_18
58: cook61_30_90_18
59: icosa6_90_18
60: jones30_90_18
61: cook61_6_90_30
62: cook61_10_90_30
63: cook61_18_90_30
64: cook61_30_90_30
65: icosa6_90_30
66: jones30_90_30
67: cook61_6_90_45
68: cook61_10_90_45
69: cook61_18_90_45
70: cook61_30_90_45
71: icosa6_90_45
72: jones30_90_45
73: cook61_6_120_12
74: cook61_10_120_12
75: cook61_18_120_12
76: cook61_30_120_12
77: icosa6_120_12
78: jones30_120_12
79: cook61_6_120_24
80: cook61_10_120_24
81: cook61_18_120_24
82: cook61_30_120_24
83: icosa6_120_24
84: jones30_120_24
85: cook61_6_120_40
86: cook61_10_120_40
87: cook61_18_120_40
88: cook61_30_120_40
89: icosa6_120_40
90: jones30_120_40
91: cook61_6_120_60
92: cook61_10_120_60
93: cook61_18_120_60
94: cook61_30_120_60
95: icosa6_120_60
96: jones30_120_60
97: all_648_72

Fig. 9. Mean, RMSD, and SD of MD, FA, HA, and |E2A| within a mid-myocardial slice averaged across subjects and plotted against nominal acquisition time. Each acquisition scheme 1–97 is encoded by color and described in the legend. For better presentation, mean values for the reference dataset labeled "all_648_72" are not plotted due to long scan time, and are instead given by black lines; 5% and 10% of the mean MD and FA from the reference dataset are indicated by red lines. *MD* mean diffusivity, *FA* fractional anisotropy, *HA* helix angle, |*E2A*| absolute sheetlet angle, *RMSD* root mean squared difference, *SD* standard deviation

were seen to be comparable to the Cook61_6 and Cook61_30 schemes, respectively. Despite our approach, which enabled systematic comparison of a relatively large number of acquisition schemes, we were limited to ND = 30 due to scan time constraints. Some advanced applications, e.g., resolving crossing fibers in the brain, require larger ND. However, our findings suggest diminishing returns in cDTI with increasing ND > 30, and there is limited evidence for higher ND, particularly where voxels with discrete crossing cell populations are limited in the myocardium. An alternative would be to employ acquisition schemes that are completely independent, as in previous pilot studies [53,54]. However, this approach extends the imaging time, limits the number of acquisition schemes that can be evaluated, and often means that datasets cannot be time-normalized. Even so, the common approach of combining all data to form a reference dataset means that reference data are not completely independent of the component data.

Table 2
RMSD and SD of MD ($\times 10^{-4}$ mm^2/s), FA, HA (°), |E2A| (°) for selected acquisition schemes, varying (top to bottom) NA_{b50}, NA_{all}, and diffusion encoding scheme (DES; mean ± SD over 10 subjects).

Vary NA_{b50}		76: Cook 61_30_120_12	82: Cook 61_30_120_24	88: Cook 61_30_120_40	94: Cook 61_30_120_60		97: Reference
RMSD	MD	0.33 ± 0.12	0.29 ± 0.09	0.27 ± 0.07	0.28 ± 0.08		0
	FA	0.028 ± 0.006	0.027 ± 0.006	0.026 ± 0.006	0.027 ± 0.006		0
	HA	6.1 ± 2.7	6.1 ± 2.7	6.2 ± 2.7	6.3 ± 2.8		0
	|E2A|	10 ± 2	10 ± 2	10 ± 2	10 ± 2		0
SD	MD	1.04 ± 0.07	0.77 ± 0.06	0.64 ± 0.05	0.55 ± 0.05		0.448 ± 0.037
	FA	0.042 ± 0.004	0.038 ± 0.004	0.036 ± 0.004	0.035 ± 0.004		0.020 ± 0.002
	HA	6.3 ± 1.5	6.3 ± 1.5	6.3 ± 1.5	6.3 ± 1.5		3.2 ± 0.9
	|E2A|	12 ± 2	12 ± 2	12 ± 2	12 ± 2		6 ± 1
Vary NA_{all}		16: Cook 61_30_30_10	40: Cook 61_30_60_20	64: Cook 61_30_90_30	88: Cook 61_30_120_40		
RMSD	MD	0.36 ± 0.11	0.30 ± 0.09	0.28 ± 0.08	0.27 ± 0.07		
	FA	0.055 ± 0.011	0.033 ± 0.007	0.028 ± 0.006	0.026 ± 0.006		
	HA	8.1 ± 2.5	6.9 ± 2.7	6.3 ± 2.5	6.2 ± 2.7		
	|E2A|	12 ± 2	11 ± 2	10 ± 2	10 ± 2		
SD	MD	1.36 ± 0.10	0.92 ± 0.07	0.74 ± 0.06	0.64 ± 0.05		
	FA	0.073 ± 0.007	0.050 ± 0.006	0.041 ± 0.005	0.036 ± 0.004		
	HA	14 ± 2	8.9 ± 1.8	7.2 ± 1.6	6.3 ± 1.5		
	|E2A|	19 ± 2	15 ± 2	13 ± 2	12 ± 2		
Vary DES		85: Cook 61_6_120_40	86: Cook 61_10_120_40	87: Cook 61_18_120_40	88: Cook 61_30_120_40	89: Icosa 6_120_40	90: Jones 30_120_40
RMSD	MD	0.52 ± 0.06	0.47 ± 0.12	0.30 ± 0.08	0.27 ± 0.07	0.52 ± 0.17	0.25 ± 0.06
	FA	0.056 ± 0.011	0.050 ± 0.010	0.035 ± 0.008	0.026 ± 0.006	0.049 ± 0.009	0.031 ± 0.009
	HA	11 ± 4	10 ± 4	7.6 ± 3.3	6.2 ± 2.7	10.6 ± 2.2	6.5 ± 2.1
	|E2A|	17 ± 2	16 ± 3	12 ± 2	10 ± 2	13 ± 2	9 ± 2
SD	MD	0.69 ± 0.06	0.68 ± 0.06	0.65 ± 0.05	0.64 ± 0.05	0.68 ± 0.05	0.68 ± 0.05
	FA	0.039 ± 0.004	0.040 ± 0.005	0.037 ± 0.005	0.036 ± 0.004	0.039 ± 0.004	0.038 ± 0.004
	HA	7.3 ± 1.9	7.3 ± 2.2	6.6 ± 1.9	6.3 ± 1.5	7.1 ± 1.2	7.1 ± 1.5
	|E2A|	12 ± 2	12 ± 2	12 ± 2	12 ± 2	11 ± 2	11 ± 2

For ease of reference, the acquisition schemes were numbered according to the legend in Fig. 9
MD mean diffusivity, *FA* fractional anisotropy, *HA* helix angle, |*E2A*| absolute sheetlet angle, *RMSD* root mean squared difference, *SD* standard deviation

6. Conclusions

In summary, we investigated the trade-off between the number of diffusion encoding directions and repetitions in M2 spin echo-based cDTI. For a given acquisition time, we found that prioritizing the number of diffusion encoding directions over NR generally yields better accuracy and precision in cDTI parameters, particularly MD and FA. We also observed that greater sampling of low b-value data improves accuracy and precision of MD and FA but not HA and |E2A|. Finally, we characterized the improvements in accuracy and precision associated with increasing the total number of acquisitions. These results may serve to guide optimization of protocols for supporting ongoing efforts in harmonization and standardization of cDTI and aid its development toward wider clinical adoption.

Funding

This work was supported by the British Heart Foundation, UK (PG/19/1/34076, CH/16/2/32089), and the Wellcome Trust (219536/Z/19/Z).

Author contributions

Sven Plein: Writing – review & editing, Supervision, Project administration, Funding acquisition. **Jürgen E. Schneider:** Writing – review & editing, Resources, Funding acquisition. **Erica Dall'Armellina:** Writing – review & editing, Supervision, Project administration, Funding acquisition. **Irvin Teh:** Writing – review & editing, Writing – original draft, Supervision, Resources, Project administration, Methodology, Investigation, Funding acquisition, Formal analysis, Data curation, Conceptualization. **Christopher Nguyen:** Writing – review & editing, Software. **David Shelley:** Writing – review & editing, Project administration, Data curation. **Sam Coveney:** Writing – review & editing, Writing – original draft, Software, Methodology, Formal analysis. **Maryam Afzali:** Writing – review & editing. **Richard J. Foster:** Writing – review & editing, Data curation. **Noor Sharrack:** Writing – review & editing, Supervision, Project administration. **Ana-Maria Poenar:** Writing – review & editing, Supervision, Project administration.

Ethics approval and consent

The study was conducted in accordance with the Declaration of Helsinki and was approved by the UK National Research Ethics Service (19/YH/0324; 18/YH/0168). All subjects provided written informed consent.

Consent for publication

Not applicable.

Availability of data and materials

The datasets used and/or analyzed during the current study are available from the corresponding author on reasonable request.

Declaration of competing interests

The authors declare that they have no known competing financial interests or personal relationships that could have appeared to influence the work reported in this paper.

Acknowledgements

We thank Siemens Healthcare for the pulse-sequence development environment. We thank Dr. Kathryn Richards for her support with the study and ethics management.

Appendix A. Supporting information

Supplementary data associated with this article can be found in the online version at doi:10.1016/j.jocmr.2025.101951.

References

[1] Dall'Armellina E, Ennis DB, Axel L, Croisille P, Ferreira PF, Gotschy A, et al. Cardiac diffusion-weighted and tensor imaging: a consensus statement from the special interest group of the Society for Cardiovascular Magnetic Resonance. J Cardiovasc Magn Reson 2025;27:101109. https://doi.org/10.1016/j.jocmr.2024.101109.

[2] Das A, Kelly C, Teh I, Stoeck CT, Kozerke S, Chowdhary A, et al. Acute microstructural changes after ST-segment elevation myocardial infarction assessed with diffusion tensor imaging. Radiology 2021;299:86–96. https://doi.org/10.1148/radiol.2021203208.

[3] Rajakulasingam R, Ferreira PF, Scott AD, Khalique Z, Azzu A, Molto M, et al. Characterization of dynamic changes in cardiac microstructure after reperfused ST-elevation myocardial infarction by biphasic diffusion tensor cardiovascular magnetic resonance. Eur Heart J 2025;46:454–69. https://doi.org/10.1093/eurheartj/ehae667.

[4] Das A, Kelly C, Teh I, Stoeck CT, Kozerke S, Sharrack N, et al. Pathophysiology of LV remodeling following STEMI: a longitudinal diffusion tensor CMR study. JACC Cardiovasc Imaging 2023;16:159–71. https://doi.org/10.1016/j.jcmg.2022.04.002.

[5] Sharrack N, Das A, Kelly C, Teh I, Stoeck CT, Kozerke S, et al. The relationship between myocardial microstructure and strain in chronic infarction using cardiovascular magnetic resonance diffusion tensor imaging and feature tracking. J Cardiovasc Magn Reson J Soc Cardiovasc Magn Reson 2022;24:66. https://doi.org/10.1186/s12968-022-00892-y.

[6] Das A, Kelly C, Teh I, Sharrack N, Stoeck CT, Kozerke S, et al. Detection of intramyocardial iron in patients following ST-elevation myocardial infarction using cardiac diffusion tensor imaging. J Magn Reson Imaging JMRI 2022;56:1171–81. https://doi.org/10.1002/jmri.28063.

[7] Das A, Kelly C, Teh I, Nguyen C, Brown LAE, Chowdhary A, et al. Phenotyping hypertrophic cardiomyopathy using cardiac diffusion magnetic resonance imaging: the relationship between microvascular dysfunction and microstructural changes. Eur Heart J Cardiovasc Imaging 2022;23:352–62. https://doi.org/10.1093/ehjci/jeab210.

[8] Ariga R, Tunnicliffe EM, Manohar SG, Mahmod M, Raman B, Piechnik SK, et al. Identification of myocardial disarray in patients with hypertrophic cardiomyopathy and ventricular arrhythmias. J Am Coll Cardiol 2019;73:2493–502. https://doi.org/10.1016/j.jacc.2019.02.065.

[9] Nielles-Vallespin S, Khalique Z, Ferreira PF, de Silva R, Scott AD, Kilner P, et al. Assessment of myocardial microstructural dynamics by in vivo diffusion tensor cardiac magnetic resonance. J Am Coll Cardiol 2017;69:661–76. https://doi.org/10.1016/j.jacc.2016.11.051.

[10] Das A, Chowdhary A, Kelly C, Teh I, Stoeck CT, Kozerke S, et al. Insight into myocardial microstructure of athletes and hypertrophic cardiomyopathy patients using diffusion tensor imaging. J Magn Reson Imaging JMRI 2021;53:73–82. https://doi.org/10.1002/jmri.27257.

[11] Joy G, Kelly CI, Webber M, Pierce I, Teh I, McGrath L, et al. Microstructural and microvascular phenotype of sarcomere mutation carriers and overt hypertrophic cardiomyopathy. Circulation 2023;148:808–18. https://doi.org/10.1161/CIRCULATIONAHA.123.063835.

[12] Gotschy A, von Deuster C, Weber L, Gastl M, Schmiady MO, van Gorkum RJH, et al. CMR diffusion tensor imaging provides novel imaging markers of adverse myocardial remodeling in aortic stenosis. JACC Cardiovasc Imaging 2021;14:1472–4. https://doi.org/10.1016/j.jcmg.2020.12.026.

[13] Gotschy A, von Deuster C, van Gorkum RJH, Gastl M, Vintschger E, Schwotzer R, et al. Characterizing cardiac involvement in amyloidosis using cardiovascular magnetic resonance diffusion tensor imaging. J Cardiovasc Magn Reson 2019;21:56. https://doi.org/10.1186/s12968-019-0563-2.

[14] Stoeck CT, von Deuster C, Genet M, Atkinson D, Kozerke S. Second-order motion-compensated spin echo diffusion tensor imaging of the human heart. Magn Reson Med 2016;75:1669–76. https://doi.org/10.1002/mrm.25784.

[15] Welsh CL, DiBella EV, Hsu EW. Higher-order motion-compensation for in vivo cardiac diffusion tensor imaging in rats. IEEE Trans Med Imaging 2015;34:1843–53. https://doi.org/10.1109/TMI.2015.2411571.

[16] von Knobelsdorff-Brenkenhoff F, Prothmann M, Dieringer MA, Wassmuth R, Greiser A, Schwenke C, et al. Myocardial T1 and T2 mapping at 3 T: reference values, influencing factors and implications. J Cardiovasc Magn Reson 2013;15:53. https://doi.org/10.1186/1532-429X-15-53.

[17] von Deuster C, Stoeck CT, Genet M, Atkinson D, Kozerke S. Spin echo versus stimulated echo diffusion tensor imaging of the in vivo human heart. Magn Reson Med 2016;76:862–72. https://doi.org/10.1002/mrm.25998.

[18] Scott AD, Ferreira PF, Nielles-Vallespin S, Gatehouse P, McGill LA, Kilner P, et al. Optimal diffusion weighting for in vivo cardiac diffusion tensor imaging. Magn Reson Med 2015;74:420–30. https://doi.org/10.1002/mrm.25418.

[19] Moulin K, Croisille P, Feiweier T, Delattre BM, Wei H, Robert B, et al. In vivo free-breathing DTI and IVIM of the whole human heart using a real-time slice-followed SE-EPI navigator-based sequence: a reproducibility study in healthy volunteers. Magn Reson Med 2016;76:70–82. https://doi.org/10.1002/mrm.25852.

[20] Jones DK. The effect of gradient sampling schemes on measures derived from diffusion tensor MRI: a Monte Carlo study. Magn Reson Med 2004;51:807–15. doi: Doi 10.1002/Mrm.20033.

[21] Wei H, Viallon M, Delattre BM, Moulin K, Yang F, Croisille P, et al. Free-breathing diffusion tensor imaging and tractography of the human heart in healthy volunteers using wavelet-based image fusion. IEEE Trans Med Imaging 2015;34:306–16. https://doi.org/10.1109/TMI.2014.2356792.

[22] Stoeck CT, von Deuster C, van Gorkum RJH, Kozerke S. Motion and eddy current-induced signal dephasing in in vivo cardiac DTI. Magn Reson Med 2020;84:277–88. https://doi.org/10.1002/mrm.28132.

[23] McClymont D, Teh I, Schneider JE. The impact of signal-to-noise ratio, diffusion-weighted directions and image resolution in cardiac diffusion tensor imaging - insights from the ex-vivo rat heart. J Cardiovasc Magn Reson 2017;19:90. https://doi.org/10.1186/s12968-017-0395-x.

[24] Lasič S, Yuldasheva N, Szczepankiewicz F, Nilsson M, Budde M, Dall'Armellina E, et al. Stay on the beat with tensor-valued encoding: time-dependent diffusion and cell size estimation in ex vivo heart. Front Phys 2022;10. https://doi.org/10.3389/fphy.2022.812115.

[25] Basser PJ, Mattiello J, Lebihan D. MR diffusion tensor spectroscopy and imaging. Biophys J 1994;66:259–67. doi: Doi 10.1016/S0006-3495(94)80775-1.

[26] Jones DK. The effect of gradient sampling schemes on measures derived from diffusion tensor MRI: a Monte Carlo study. Magn Reson Med 2004;51:807–15. https://doi.org/10.1002/mrm.20033.

[27] Landman BA, Farrell JA, Jones CK, Smith SA, Prince JL, Mori S. Effects of diffusion weighting schemes on the reproducibility of DTI-derived fractional anisotropy, mean diffusivity, and principal eigenvector measurements at 1.5T. NeuroImage 2007;36:1123–38. https://doi.org/10.1016/j.neuroimage.2007.02.056.

[28] Sairanen V, Kuusela L, Sipila O, Savolainen S, Vanhatalo S. A novel measure of reliability in diffusion tensor imaging after data rejections due to subject motion. NeuroImage 2017;147:57–65. https://doi.org/10.1016/j.neuroimage.2016.11.061.

[29] Jones DK, Basser PJ. "Squashing peanuts and smashing pumpkins": how noise distorts diffusion-weighted MR data. Magn Reson Med 2004;52:979–93. https://doi.org/10.1002/mrm.20283.

[30] Farrell JA, Landman BA, Jones CK, Smith SA, Prince JL, van Zijl PC, et al. Effects of signal-to-noise ratio on the accuracy and reproducibility of diffusion tensor imaging-derived fractional anisotropy, mean diffusivity, and principal eigenvector measurements at 1.5 T. J Magn Reson Imaging JMRI 2007;26:756–67. https://doi.org/10.1002/jmri.21053.

[31] Ni H, Kavcic V, Zhu T, Ekholm S, Zhong J. Effects of number of diffusion gradient directions on derived diffusion tensor imaging indices in human brain. AJNR Am J Neuroradiol 2006;27:1776–81.

[32] Zhan L, Jahanshad N, Ennis DB, Jin Y, Bernstein MA, Borowski BJ, et al. Angular versus spatial resolution trade-offs for diffusion imaging under time constraints. Hum Brain Mapp 2013;34:2688–706. https://doi.org/10.1002/hbm.22094.

[33] Scott AD, Ferreira P, Nielles-Vallespin S, McGill LA, Pennell DJ, Firmin D. Directions vs. averages: an in-vivo comparison for cardiac DTI. J Cardiovasc Magn Reson 2015;17(1):P25. https://doi.org/10.1186/1532-429X-17-S1-P25.

[34] Cork TE, Hannum AJ, Middione MJ, Ennis D. Trading off averages and directions for cardiac diffusion tensor imaging. Paper/Poster presented at: Proceedings of the International Society for Magnetic Resonance in Medicine; 2023; Toronto, Canada.

[35] Teh I, Nguyen C, Kelly C, Da E, Li D, Plein S, et al. Optimisation of diffusion encoding schemes for in vivo cardiac DTI. Paper/Poster presented at: Proceedings of the International Society for Magnetic Resonance in Medicine; 2019; Montreal, Canada.

[36] Teh I, Kelly C, Shelley D, Poenar AM, Plein S, Da E, et al. In vivo clinical cardiac DTI in 5 min. Paper/Poster presented at: Proceedings of the International Society for Magnetic Resonance in Medicine; 2022; London, UK.

[37] Jones DK, Horsfield MA, Simmons A. Optimal strategies for measuring diffusion in anisotropic systems by magnetic resonance imaging. Magn Reson Med 1999;42:515–25.

[38] Cook PA, Symms M, Boulby PA, Alexander DC. Optimal acquisition orders of diffusion-weighted MRI measurements. J Magn Reson Imaging 2007;25:1051–8. https://doi.org/10.1002/jmri.20905.

[39] Skare S, Hedehus M, Moseley ME, Li TQ. Condition number as a measure of noise performance of diffusion tensor data acquisition schemes with MRI. J Magn Reson 2000;147:340–52. https://doi.org/10.1006/jmre.2000.2209.

[40] Akkerman EM. Efficient measurement and calculation of MR diffusion anisotropy images using the Platonic variance method. Magn Reson Med 2003;49:599–604. https://doi.org/10.1002/mrm.10365.

[41] Coveney S, Afzali M, Mueller L, Teh I, Das A, Dall'Armellina E, et al. Outlier detection in cardiac diffusion tensor imaging: Shot rejection or robust fitting? Med Image Anal 2025;101:103386. https://doi.org/10.1016/j.media.2024.103386.

[42] Garyfallidis E, Brett M, Amirbekian B, Rokem A, van der Walt S, Descoteaux M, et al. Dipy, a library for the analysis of diffusion MRI data. Front Neuroinform 2014;8:8. https://doi.org/10.3389/fninf.2014.00008.

[43] Lowekamp BC, Chen DT, Ibanez L, Blezek D. The design of SimpleITK. Front Neuroinform 2013;7:45. https://doi.org/10.3389/fninf.2013.00045.

[44] Dietrich O, Raya JG, Reeder SB, Reiser MF, Schoenberg SO. Measurement of signal-to-noise ratios in MR images: influence of multichannel coils, parallel imaging, and reconstruction filters. J Magn Reson Imaging JMRI 2007;26:375–85. https://doi.org/10.1002/jmri.20969.

[45] Salvador R, Pena A, Menon DK, Carpenter TA, Pickard JD, Bullmore ET. Formal characterization and extension of the linearized diffusion tensor model. Hum Brain Mapp 2005;24:144–55. https://doi.org/10.1002/hbm.20076.
[46] Ferreira PF, Kilner PJ, McGill LA, Nielles-Vallespin S, Scott AD, Ho SY, et al. In vivo cardiovascular magnetic resonance diffusion tensor imaging shows evidence of abnormal myocardial laminar orientations and mobility in hypertrophic cardiomyopathy. J Cardiovasc Magn Reson 2014;16:87. https://doi.org/10.1186/S12968-014-0087-8.
[47] Chung S, Lu Y, Henry RG. Comparison of bootstrap approaches for estimation of uncertainties of DTI parameters. NeuroImage 2006;33:531–41. https://doi.org/10.1016/j.neuroimage.2006.07.001.
[48] Teh I, Romero RW, Boyle J, Coll-Font J, Dall'Armellina E, Ennis DB, et al. Validation of cardiac diffusion tensor imaging sequences: a multicentre test-retest phantom study. NMR Biomed 2022;35:e4685. https://doi.org/10.1002/nbm.4685.
[49] Aliotta E, Moulin K, Magrath P, Ennis DB. Quantifying precision in cardiac diffusion tensor imaging with second-order motion-compensated convex optimized diffusion encoding. Magn Reson Med 2018;80:1074–87. https://doi.org/10.1002/mrm.27107.
[50] Holm S. A simple sequentially rejective multiple test procedure. Scand J Stat 1979;6:65–70.
[51] Caruyer E, Lenglet C, Sapiro G, Deriche R. Design of multishell sampling schemes with uniform coverage in diffusion MRI. Magn Reson Med 2013;69:1534–40. https://doi.org/10.1002/mrm.24736.
[52] Coveney S, Afzali M, Mueller L, Teh I, Das A, Dall'Armellina E, et al. Outlier detection in cardiac diffusion tensor imaging: shot rejection or robust fitting? Med Image Anal 2024;101:103386. https://doi.org/10.1016/j.media.2024.103386.
[53] Scott AD, Ferreira P, Nielles-Vallespin S, McGill LA, Pennell D, Firmin DN. Directions vs. averages: an in-vivo comparison for cardiac DTI. Paper/Poster presented at: 18th Annual SCMR; 2015.
[54] Mazumder R, Clymer BD, White RD, Kolipaka A. Estimation of helical angle of the left ventricle using diffusion tensor imaging with minimum acquisition time. Paper/Poster presented at: 17th Annual SCMR; 2014.
[55] Teh I, McClymont D, Burton RA, Maguire ML, Whittington HJ, Lygate CA, et al. Resolving fine cardiac structures in rats with high-resolution diffusion tensor imaging. Sci Rep 2016;6:30573. https://doi.org/10.1038/srep30573.
[56] Afzali M, Mueller L, Coveney S, Fasano F, Evans CJ, Engel M, et al. In vivo diffusion MRI of the human heart using a 300 mT/m gradient system. Magn Reson Med 2024;92:1022–34. https://doi.org/10.1002/mrm.30118.
[57] Scott AD, Nielles-Vallespin S, Ferreira PF, McGill LA, Pennell DJ, Firmin DN. The effects of noise in cardiac diffusion tensor imaging and the benefits of averaging complex data. NMR Biomed 2016;29:588–99. https://doi.org/10.1002/nbm.3500.
[58] Eichner C, Cauley SF, Cohen-Adad J, Moller HE, Turner R, Setsompop K, et al. Real diffusion-weighted MRI enabling true signal averaging and increased diffusion contrast. NeuroImage 2015;122:373–84. https://doi.org/10.1016/j.neuroimage.2015.07.074.
[59] Chuang JS, Zemljic-Harpf A, Ross RS, Frank LR, McCulloch AD, Omens JH. Determination of three-dimensional ventricular strain distributions in gene-targeted mice using tagged MRI. Magn Reson Med 2010;64:1281–8. https://doi.org/10.1002/mrm.22547.
[60] Lau AZ, Tunnicliffe EM, Frost R, Koopmans PJ, Tyler DJ, Robson MD. Accelerated human cardiac diffusion tensor imaging using simultaneous multislice imaging. Magn Reson Med 2015;73:995–1004. https://doi.org/10.1002/mrm.25200.
[61] Teh I, McClymont D, Carruth E, Omens J, McCulloch A, Schneider JE. Improved compressed sensing and super-resolution of cardiac diffusion MRI with structure-guided total variation. Magn Reson Med 2020;84:1868–80. https://doi.org/10.1002/mrm.28245.
[62] Wu Y, Zhu YJ, Tang QY, Zou C, Liu W, Dai RB, et al. Accelerated MR diffusion tensor imaging using distributed compressed sensing. Magn Reson Med 2014;71:763–72. https://doi.org/10.1002/mrm.24721.
[63] Phipps K, van de Boomen M, Eder R, Michelhaugh SA, Spahillari A, Kim J, et al. Accelerated in vivo cardiac diffusion-tensor MRI using residual deep learning-based denoising in participants with obesity. Radiol Cardiothorac Imaging 2021;3:e200580. https://doi.org/10.1148/ryct.2021200580.
[64] Weine J, van Gorkum RJH, Stoeck CT, Vishnevskiy V, Kozerke S. Synthetically trained convolutional neural networks for improved tensor estimation from free-breathing cardiac DTI. Comput Med Imaging Graph 2022;99:102075. https://doi.org/10.1016/j.compmedimag.2022.102075.
[65] Huang J, Ferreira PF, Wang L, Wu Y, Aviles-Rivero AI, Schonlieb CB, et al. Deep learning-based diffusion tensor cardiac magnetic resonance reconstruction: a comparison study. Sci Rep 2024;14:5658. https://doi.org/10.1038/s41598-024-55880-2.
[66] Liu S, Liu Y, Xu X, Chen R, Liang D, Jin Q, et al. Accelerated cardiac diffusion tensor imaging using deep neural network. Phys Med Biol 2023;68:025008. https://doi.org/10.1088/1361-6560/acaa86.
[67] Coll-Font J, Chen S, Eder R, Fang Y, Han QJ, van den Boomen M, et al. Manifold-based respiratory phase estimation enables motion and distortion correction of free-breathing cardiac diffusion tensor MRI. Magn Reson Med 2022;87:474–87. https://doi.org/10.1002/mrm.28972.
[68] van Gorkum RJH, Guenthner C, Koethe A, Stoeck CT, Kozerke S. Characterization and correction of diffusion gradient-induced eddy currents in second-order motion-compensated echo-planar and spiral cardiac DTI. Magn Reson Med 2022;88:2378–94. https://doi.org/10.1002/mrm.29378.
[69] Scholten H, Wech T, Kohler S, Smart SS, Boyle JH, Teh I, et al. On the correction of spiral trajectories on a preclinical MRI scanner with a high-performance gradient insert. NMR Biomed 2024;37:e5249. https://doi.org/10.1002/nbm.5249.
[70] Nguyen CT, Christodoulou AG, Coll-Font J, Ma S, Xie Y, Reese TG, et al. Free-breathing diffusion tensor MRI of the whole left ventricle using second-order motion compensation and multitasking respiratory motion correction. Magn Reson Med 2021;85:2634–48. https://doi.org/10.1002/mrm.28611.